# Mueller Matrix Polarimetry in Biomedicine: Enabling Technology, Biomedical Applications, and Future Prospects


**Michael D. Singh, Nirmalya Ghosh, and I. Alex Vitkin**

## 1 Introduction

The prospect of evaluating media without destroying or otherwise disturbing its properties has long been sought and readily adopted in biomedicine and beyond. Low-intensity light has played a particularly important role in the field of non-destructive evaluation (NDE) due to its rather unobtrusive interaction with matter, along with its numerous versatile properties that can carry important information about interrogated media. Indeed, the field of diagnostic biomedical optics has seen powerful exploitations of light, relying on its intensity (brightness) for imaging and wavelength (colour) for spectroscopy. Somewhat less prevalent but nevertheless actively researched and occasionally accepted into the NDE arsenal are field properties of the light wave, namely, its amplitude and phase, coherence, and polarization. In fact, these field properties, coherence and polarization, are more fundamental and have played important roles in our understanding of the transverse character of the electromagnetic wave, angular momentum of light or photons, and a number of non-trivial optical phenomena related to the interference of light waves.

The polarization property of light, which describes the oscillatory nature of its electric or magnetic fields, however, has far from reached its potential in

M. D. Singh (✉)
Department of Medical Biophysics, University of Toronto, Toronto, ON, Canada
e-mail: MichaelDhillon.Singh@mail.utoronto.ca

N. Ghosh
Department of Physical Sciences, Indian Institute of Science Education and Research Kolkata, Mohanpur, West Bengal, India

I. A. Vitkin
Department of Radiation Oncology, University of Toronto, Toronto, ON, Canada

Division of Biophysics and Bioimaging, Princess Margaret Cancer Centre, Toronto, ON, Canada



J. C. Ramella-Roman, T. Novikova (eds.), *Polarized Light in Biomedical Imaging and Sensing*, https://doi.org/10.1007/978-3-031-04741-1_3

biomedicine. This may come as a surprise since polarimetry – the science of measuring light's polarization and its interaction with matter – has been actively studied for more than two centuries [1] and has already enjoyed successful deployment in the semiconductor industry as an NDE tool for many decades [2]. The powerful potential of polarimetry in biomedicine arises from the well-known polarimetric effects of tissues, namely, linear retardance and diattenuation due to linear birefringent and dichroic microstructures, optical activity (circular retardance and circular diattenuation) due to chiral structures, and depolarization primarily due to multiple scattering and other randomization effects – all of which have been demonstrated to carry important tissue information and have found important early applications [3]. However, depolarization is both a blessing and a curse for tissue polarimetry: while potentially of diagnostic value, its effect can be overwhelming due to the complex heterogeneous nature of tissues such that polarized light signals are effectively extinguished (bulk tissue depolarization), thereby seriously hindering polarimetry's adoption in biomedicine. There are, however, recent promising developments of new technologies and methodologies that can detect the often faint polarimetric signals, and thus extract fruitful tissue information. These advances have especially revived the interest in measuring Mueller matrices, which comprehensively describe the polarization properties of interrogated materials.

**The Rise of Mueller Matrix Polarimetry in Biomedicine**

In 1852, Sir George Gabriel Stokes introduced four measurable *intensity* quantities, now known as Stokes parameters, which completely described and enabled the observation of the *polarization behaviour of light* [4]. The Stokes parameters of both incident and scattered (post-interaction) light from a medium can then be related through a $4 \times 4$ matrix which fully encapsulate *the medium's polarization response*. These matrices were first formulated by Paul Soleillet in his 1929 thesis [5]; the calculus of the matrices was introduced by Francis Perrin in 1942 [6], and then developed in considerable detail by Hans Mueller beginning in 1943 [7], thus earning the name 'Mueller matrix' (MM) [8]. In parallel, Robert Clark Jones also developed a polarization matrix calculus in 1941 in a series of papers based on a field formulation (*amplitude* and *phase*) [9–12]. Jones calculus has remained fundamentally important, specifically in the context of establishing a link between the classical description of the polarization of electromagnetic waves and the fundamentally much richer quantum mechanical description of the polarization state vector for the photon. It is however limited to completely polarized light interactions and is not readily adaptable for describing depolarization events that occur in most heterogeneous materials such as biological tissues; thus, Jones matrix calculus has been largely supplanted by the more powerful and experimentally applicable Mueller matrix calculus [8].

Early uses of MM polarimetry included compositional analysis of atmosphere [13] and seawater [14], as well as astronomical observation [15, 16]. In biology, a seminal paper in 1976 by Bickel et al. [17] reported on a 'new biophysical tool' referring to their Mueller measurements of cells suspended in liquid, whose

elements provided information related to cellular structure and size. These early Mueller applications used previously existing technologies adapted to polarimetric implementations, such as nephlometers and photometers, or new technologies altogether. For example, the latter cellular study was enabled by a sensitive new device known as the photoelastic modulator (PEM) [18, 19], used in tandem with lock-in amplification for synchronous high-SNR detection of polarized light. It became obvious that Mueller polarimetry, with the help of developing technology, afforded useful NDE information about scattering media, potentially suitable for biomedical diagnostics.

Interest then arose in using MM polarimetry towards assessment of biological tissues, particularly for pathological detection; however, the complexity of biological media and severe polarization loss were problematic, and thus many initial biomedical studies were limited to cell suspensions [20] and turbid phantoms which mimicked tissue scattering (e.g. microsphere suspensions) [21–24]. One of the first MM measurements of actual tissue were those of human eyes *post-mortem* by Dreher et al. in 1992 [25], benefitting from the reduced multiple scattering and less complex polarization effects in such nearly transparent ocular media. The authors discussed the detection of glaucoma and other optic neuropathies by measuring the linear retardance, optic-axis orientation, and linear dichroism of retinal nerve fibres. More complex tissues which (1) cause extensive polarization loss and (2) exhibit multiple polarimetric effects simultaneously (e.g. depolarization, linear/circular birefringence, and dichroism) posed a greater challenge for MM polarimetry on both measurement (1) and analysis (2) fronts. With respect to the latter, since the MM is a polarization transfer function which effectively 'lumps' all the polarimetric effects of the interacting media in a complex way into its 16 elements, additional interpretation methods must be applied to the resultant MMs to tease these out individually. Numerous interpretation methods have been introduced in recent decades, based on various forms of matrix decomposition [26–29]. The polar decomposition approach proposed by Lu and Chipman [30] in 1996 was the first method applied to MM polarimetry of tissue in a 2000 study by Smith et al. [31] which identified cancerous and lupus lesions of the skin. It remains arguably the most common MM decomposition method in tissue polarimetry at present, but the matter is not settled and active research into this interesting avenue of inquiry continues to this day [32, 33].

Since these early studies, technologies and methodologies have progressed to enable more advanced demonstrations of tissue assessment through MM polarimetry in various biomedical scenarios, for example, (pre)cancer [34], bladder obstruction [35, 36], infarcted and stem-cell-regenerated myocardium [37], and glucose sensing [38–41]. Both thin-tissue transmission methods and bulk-tissue reflection geometries have been attempted, with the latter being more challenging due to greater depolarizing noise but also more biomedically relevant for eventual in-vivo clinical deployment. These demonstrations have mostly used free-space optics, since performing MM polarimetry through flexible fibre optics (e.g. medical endoscopes) introduces the significant artefact of large and variable fibre-induced strain birefringence. Using rigid endoscopes prevents such probe noise from drowning out

the tissue polarization signature, but rigid endoscopy is limited in its clinical scope [42]. Recent developments in advanced normalization methods for flexible MM endoscopy have also shown some promise [43–45]; if clinically realized, this fibre-optic-based approach may prove impactful by opening up previously inaccessible anatomical sites in the context of surgical guidance, early detection, diagnostics, and surveillance.

An interesting overall system design consideration is whether polarimetry (or any NDE diagnostic technique for that matter) should be used as a stand-alone modality or be combined with another interrogation technique that carries additional (and ideally complimentary) tissue information. The 'correct' decision on stand-alone versus hybrid approaches is clearly dependent on the biomedical information being sought, potential complementarity of the candidate techniques, technological complexity, and so on. This is particularly relevant to polarized light NDE, as some polarimetric implementations are technologically simple, and thus can be readily placed into the existing optical paths of other optical modalities, adding rich polarimetric information at 'minimal cost'. Thus, hybrid optical approaches have been demonstrated which implement MM polarimeters in combination with multispectral imaging [46–48], optical coherence tomography (OCT) [49–52], microscopy [53], mass spectrometry [54, 55], and possibly others.

MM polarimetry is driven by unmet scientific and clinical needs and is very much dependent on emerging state-of-the-art technologies and methodologies to enable various exciting applications in biomedicine, with promise to join the rank of the other more established biophotonics-based diagnostic techniques. This chapter reviews the current and prospective biomedical applications of MM polarimetry, along with the enabling technological advances that can further improve and realize potential exciting uses in the life sciences.

## 2 Mueller Polarimetry: Concepts and Methods

### *2.1 What Is Polarized Light?*

In classical electromagnetic theory, polarization of light is described through the evolution of transverse electric ($\boldsymbol{E}$) and magnetic ($\boldsymbol{B}$) fields as a function of time at a given point in space. The $\boldsymbol{E}$ and the $\boldsymbol{B}$ fields sinusoidally oscillate in the $xy$ plane, while the wave vector ($\boldsymbol{\beta}$) is directed along the propagation direction, $z$-axis. Since the triplet of vectors $\boldsymbol{E}$, $\boldsymbol{B}$, and $\boldsymbol{\beta}$ are mutually orthogonal, it suffices to look only at the behaviour of the vector $\boldsymbol{E}$. The wave may be considered as the superposition of two waves having orthogonal components $E_x$ and $E_y$ as

$$\boldsymbol{E}\,(z,t) = \boldsymbol{E_x}\,(z,t) + \boldsymbol{E_y}\,(z,t)\,, \tag{1}$$

with

$$\boldsymbol{E_x}(z,t) = E_{0x}\cos(\omega t - \beta z + \phi_x)\,\hat{\boldsymbol{x}}, \tag{2}$$

$$\boldsymbol{E_y}(z,t) = E_{0y}\cos\left(\omega t - \beta z + \phi_y\right)\hat{\boldsymbol{y}}, \tag{3}$$

and

$$\beta = \frac{2\pi n}{\lambda} \text{ and } \omega = 2\pi f, \tag{4}$$

where $\lambda$ is the wavelength of light, $n$ is the refractive index of the host medium, $f$ is the oscillation frequency of the monochromatic electric field, and $\phi$ is the phase. If the trace of the vector extremity $\boldsymbol{E}$ follows a stationary curve in their temporal evolution, the wave is said to be completely polarized. Accordingly, the shape of the curve traced out by $\boldsymbol{E}$ vector defines the polarization state of the wave. The electric field vector, $\boldsymbol{E}$, traces out an ellipse through space whose shape may vary between perfectly linear or perfectly circular forms. Note that in the corresponding quantum mechanical description, it is assumed that each individual photon is polarized, and its associated state vector corresponds to one of the classical polarization states described by the Jones vector. In the limit of a large number of photons, their collective behaviour is consistent with the classical description of polarization ellipse. Though this polarization ellipse may describe light's polarization, it becomes impractical due to its dependency on the amplitude of $\boldsymbol{E}$ which is traced at the frequency of the light's electric field oscillation, on the order of $10^{-15}$ s. Furthermore, the polarization ellipse is applicable only to completely polarized and perfectly coherent light waves – an exception rather that the rule in most practical applications – and thus in order to describe partially or completely unpolarized light, one needs to incorporate the decoherence effect through time averaged and practically measurable quantities such as intensity of light. A more suitable formalism thus describes the *degree of polarization* (DOP) of light which ranges from completely unpolarized to completely polarized using directly observable and measurable polarization resolved intensities.

## 2.2 Stokes Vectors: Describing Polarized Light

Polarization behaviour is observable by using polarization modulating elements in certain configurations to measure the resultant time-averaged intensity (the square of the electric field) rather than the rapidly revolving electric field amplitude and the associated phase. Stokes vectors do just that by using linear and circular polarizers/analysers. Specifically, the difference in intensities between orthogonal linear and circular polarization states is measured and compared to the values of

total light intensity in order to quantify the linear, circular, and total DOPs. Note that Stokes vectors are not 'magnitude + direction' vectors in the conventional sense but are simply $4 \times 1$ arrays of real-valued numbers. The Stokes vector may however be represented as a directional vector in the polarization state space, in the so-called Poincaré sphere (not discussed here). They consist of four measurable quantities (Stokes parameters) which are the total intensity $I$, the amount of linear horizontal or vertical polarization $Q$, the amount of linear $+45^\circ$ or $-45^\circ$ polarization $U$, and the amount of right-circular or left-circular polarization $V$:

$$S = \begin{bmatrix} I \\ Q \\ U \\ V \end{bmatrix} = \begin{bmatrix} I_{\parallel} + I_{\perp} \\ I_{\mathrm{H}} - I_{\mathrm{V}} \\ I_{+45} - I_{-45} \\ I_{\mathrm{R}} - I_{\mathrm{L}} \end{bmatrix}, \tag{5}$$

where $I_{\mathrm{H}}$, $I_{\mathrm{V}}$, $I_{+45}$, $I_{-45}$, $I_{\mathrm{R}}$, and $I_{\mathrm{L}}$ are the light intensities measured by a horizontal linear analyser, a vertical linear analyser, a linear analyser oriented at $+45^\circ$, a linear analyser oriented at $-45^\circ$, a right circular analyser, and a left circular analyser before reaching the detector, respectively. Additionally, $I_{\parallel}$ and $I_{\perp}$ are any two mutually orthogonal polarization states.

The degrees of linear, circular, and total light polarization can be calculated using the Stokes parameters according to

$$\mathrm{DOP_L} = \frac{\sqrt{Q^2 + U^2}}{I}, \tag{6}$$

$$\mathrm{DOP_C} = \frac{\sqrt{V^2}}{I}, \tag{7}$$

$$\mathrm{DOP} = \frac{\sqrt{Q^2 + U^2 + V^2}}{I}. \tag{8}$$

Importantly, Stokes vectors describe the polarization state of the light, but they do not describe the polarization properties of an interacting material.

## 2.3 Mueller Matrix: Describing Material Polarization Properties

The polarization states of light before and after their interaction with a medium are represented by Stokes vectors. A Mueller matrix, $M$, describes the polarimetric characteristics of the interacting medium and relates the incident and post-interaction Stokes vectors through

$$S_{\text{out}} = \begin{bmatrix} I \\ Q \\ U \\ V \end{bmatrix}_{\text{out}} = \begin{bmatrix} M_{11} & M_{12} & M_{13} & M_{14} \\ M_{21} & M_{22} & M_{23} & M_{24} \\ M_{31} & M_{32} & M_{33} & M_{34} \\ M_{41} & M_{42} & M_{34} & M_{44} \end{bmatrix} \times \begin{bmatrix} I \\ Q \\ U \\ V \end{bmatrix}_{\text{in}} = M \cdot S_{\text{in}}. \tag{9}$$

Encapsulated within the MM are all the polarization properties of a sample, namely diattenuation, polarizance, retardance, and depolarization. As such, when tissue is interrogated by polarized light, the measured MM will contain all possible obtainable information about it. Such information includes the material properties described below.

*Polarizance* refers to a material's ability to increase the DOP of light, whereas *diattenuation* occurs when an interacting medium attenuates the orthogonal components of light's electric field unequally, resulting in preferential transmittance of a certain polarization orientation. The former is described in the Mueller matrix's first column $[M_{11}\ M_{21}\ M_{31}\ M_{41}]^T$ and the latter by the first row $[M_{11}\ M_{12}\ M_{13}\ M_{14}]$. These effects generally occur at material interfaces where the transmittance and reflectance are dependent upon the incident polarization state or in anisotropic materials that preferentially absorb certain polarization states such as linearly or circularly polarized light (referred to as *linear* and *circular dichroism*, respectively). Single scattering is also known to impart polarizance and diattenuation signatures on polarized light when observed at certain angles in a scattering plane.

*Retardance* occurs when a medium alters the phase-difference between the orthogonal components of light's electric field, represented by the sub-matrix $[M_{22}\ M_{23}\ M_{24}; M_{32}\ M_{33}\ M_{34}; M_{42}\ M_{43}\ M_{44}]$. Materials that produce this effect are known as *birefringent*. Note that retardance and diattenuation are the result of differences in the refractive indices for different polarization states. These are described through the ordinary and extraordinary axes and indices. Difference in the real parts of the said indices result in linear and circular birefringence (retardance or phase difference between orthogonal polarizations), while the difference in the imaginary parts gives rise to the linear and circular dichroism (diattenuation or differential attenuation of orthogonal polarizations). Generally, fibrous tissues such as collagen and tendons are linearly birefringent. As noted above, circular retardance, commonly referred to as *optical activity*, then affects the phase-difference between those circular states. This process maintains the light's linear ellipticity, rotating its plane about the propagation axis by an angle proportional to the *rotatory power* of the material. Glucose – an essential molecule for life – is *chiral* and thus optically active, allowing polarized light to probe its molecular concentrations (as has been routinely done in the sugar industry (glucometry) [56, 57]).

*Depolarization* refers to the scrambling of the photon polarizations which comprise a light beam. Materials generally depolarize light via multiple scattering which occurs at inter-medium interfaces that bring about abrupt changes to the refractive index, possibly randomizing the polarization orientation of the interacting photons. Scattering occurs in virtually all biotissues due their heterogeneous structure and composition. Depolarization may also occur in birefringent media with randomly

oriented microdomains that act as incremental retarders to randomize the phases of incident photons [58]. Depolarization can thus be a useful metric in probing tissues due to its prevalence, albeit when its effects are manageable. A material that depolarizes light is known as a depolarizer. An ideal depolarizer has MM of the form:

$$M_{\mathrm{D}} = \begin{bmatrix} 1 & 0 & 0 & 0 \\ 0 & a & 0 & 0 \\ 0 & 0 & b & 0 \\ 0 & 0 & 0 & c \end{bmatrix}, \tag{10}$$

where $|a|$, $|b|$, $|c|$ are all $\leq 1$. Thus, the Stokes vector of light, $S_{\mathrm{in}}$, incident upon the depolarizer will be transformed to $S_{\mathrm{out}}$ as

$$S_{\mathrm{out}} = M_{\mathrm{D}} \cdot S_{\mathrm{in}} = \begin{bmatrix} I \\ aQ \\ bU \\ cV \end{bmatrix}_{\mathrm{out}}, \tag{11}$$

where $\mathrm{DOP}_{\mathrm{out}} \leq \mathrm{DOP}_{\mathrm{in}}$.

These polarimetric effects occur simultaneously in complex media such as biological tissues and are thus 'lumped' into a single Mueller matrix. Therefore, suitable interpretation methods must be employed to decouple the effects and provide meaningful biophysical information. Polar decomposition proposed by Lu and Chipman [30] has been used extensively in Mueller bio-polarimetry whereby it serially decomposes a resultant Mueller matrix into an ordered sequence of depolarizer, retarder, and diattenuation sub-matrices, enabling separate extraction of these tissue properties. Other alternatives such as differential decomposition [26] model polarimetric effects more realistically as continuously occurring during light propagation rather than sequentially. It however relies on logarithmic operations which are formidable when employing reflectance configurations due to resultant negative eigenvalues of Mueller matrix elements (e.g. helicity-flipping [21]). There are also emerging interpretation methods such as Mueller transformation [59, 60] and machine learning [61–63] that may enable improved extraction of novel polarimetric parameters.

## 2.4 Mueller Matrix Measurement

In order to measure the Mueller matrix of a sample, the incident and post-interaction light must be modulated with certain polarization states using a polarization state generator (PSG) and polarization state analyser (PSA), respectively, before impinging onto a detector. To determine the complete $4 \times 4$ matrix, four polarization

states must be generated and analysed, out of the six possible ones: vertical (V) linear, horizontal (H) linear, $+45°$ ($P^+$) and $-45°$ ($P^-$) linear, and right- (R), and left-circular (L). For example, using the four states H, V, $P^+$, and R, a 'data matrix' (not a Mueller matrix) may be acquired [58]:

$$\begin{bmatrix} HH & HV & HP^+ & HR \\ VH & VV & VP^+ & VR \\ P^+H & P^+V & P^+P^+ & P^+R \\ RH & RV & RP^+ & RR \end{bmatrix}, \tag{12}$$

where the first and second symbols, respectively, indicate the generated and analysed polarization states; for example, VH is the signal when vertical linear polarization generated by the PSG illuminates the sample and the remitted light is sampled through horizontal linear polarization orientation of the PSA. From the data matrix, the Mueller matrix may be determined by an algorithm, such as the one introduced by Yao and Wang [49].

A schematic view of the general MM measurement scheme using four such states is shown in Fig. 1. The classical (and simplest) method to generate and analyse polarization states is by discrete settings of linear polarizers and phase retarders (e.g. quarter wave plates). This is however slow, cumbersome, and susceptible to error when adjusted manually. Thus, more advanced devices have been developed that operate as a function of time (dynamic modulation) or in the spectral/spatial domain. The former is generally achieved through dynamic retarding components

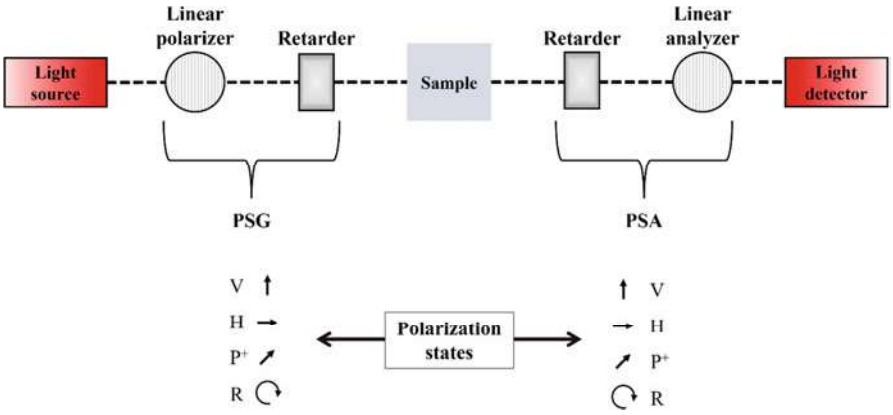


**Fig. 1** General setup for measuring the Mueller matrix of a sample. A polarization state generator (PSG) generates different polarization states of light that are incident on the sample. The post-interaction light is analysed using a polarization state analyser with its components in the opposite order of the PSG before transmitting to a light intensity detector. In this example, four polarization states are generated and analysed to produce a data matrix (see Eq. 12) from which the Mueller matrix is determined using a suitable algorithm. Transmission geometry is shown for illustrative purposes only

such as motor-rotated quarter wave plates, PEMs, and liquid crystal retarders. PEMs typically consist of transparent slabs of quartz which are compressed and stretched periodically to produce a time-varying strain birefringence; thus, incident $+45^{\circ}$ linearly polarized light will have its polarization state periodically and continuously varying between unaltered $+45^{\circ}$ linear (when PEM strain $= 0$) and elliptical/circular (when PEM strain is set to its user-controlled maximum). Importantly, a lock-in amplifier can then be used to 'lock-in' on the PEM modulation frequency and its harmonic to synchronously detect polarized light signals amid significant backgrounds of depolarized 'noise' (thus enabling high SNR detection). Liquid crystal cells are also controlled electronically whereby the orientation of its molecules are modulated by an applied voltage, changing its birefringence, and thus dynamically retarding the phase of incident polarized light. These two devices are advantageous for tissue polarimetry since they are electronically controlled with no moving parts (robust) and exhibit millisecond response times (minimizing motion artefacts). Alternatively, so-called snapshot systems modulate polarized light using diffractive elements to generate interference fringes which can be analysed via Fourier analysis in the frequency domain. Comparatively speaking, snapshot systems perform the fastest Mueller measurements, however at the cost of limited image resolution [64].

Spectroscopic polarimeters yield polarization signatures as a function of wavelength and may offer additional insights in biomedicine such as early detection of epithelial cancers (based on a wavelength-dependent oscillatory component of backscattered light) [65, 66]. An interesting extension of this approach is to also measure polarization of the fluorescence emission which can provide biochemical information [67]. A representative system is illustrated in Fig. 2. For elastic scattering measurements, a broadband light source, such as a Xe lamp is used, while for fluorescence spectroscopic measurements, laser sources having desirable excitation wavelengths are used. As per above, the Mueller matrix measurement strategy is based on 16 (spectrally resolved) intensity measurements performed by sequentially generating and analysing four elliptical polarization states. This approach enables recording of spectroscopic Mueller matrices MM($\lambda$) over a broad spectral range (e.g. $\lambda = 400$–$800$ nm) with high accuracy and sensitivity. For MM fluorescence spectroscopy, the samples are excited with a chosen wavelength (e.g. $\lambda_{ex} = 405$), and the emitted fluorescence spectra from the sample are recorded by a spectrometer (e.g. $\lambda_{em} = 450 - 750$ nm). An important point is that the generator matrix corresponding to the excitation wavelength is used and the analyser matrices are taken for the entire emission wavelengths. Results of fluorescence spectroscopic measurements from biological tissues using this experimental system are presented and discussed later.

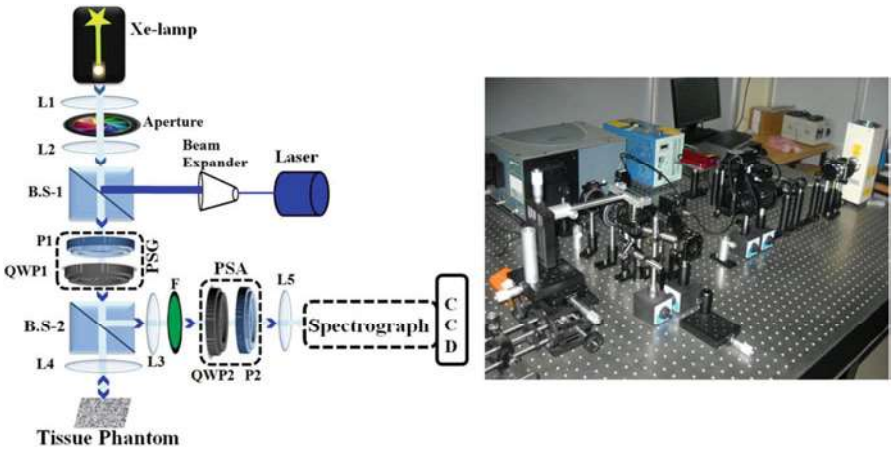


**Fig. 2** Schematic of the experimental systems for elastic scattering and fluorescence Mueller matrix measurements in the exact backscattering configuration. P1 and P2 are linear polarizers; QWP1 and QWP2 are rotatable achromatic quarter wave plates; L1, L2, L3, L4, and L5 are lenses; BS-1 and BS-2 are beam splitters. P1, QWP1 form the PSG unit and P2, QWP2 form the PSA unit. The Xe-lamp is used as the excitation source for recording elastic scattering spectral Mueller matrices, whereas the 405 nm line of a diode laser is used as the excitation source for recording fluorescence spectral Mueller matrices. A long pass filter F is used to block the laser line for fluorescence measurements. A photograph of the experimental system is shown on the right

## *2.5 Experimental Design and Information Content Considerations*

Polarimetry is a flexible NDE technique that can be implemented in many ways to extract useful information about biological tissues, with pros and cons associated with each implementation. For example, one must consider the polarization modulation/detection system and measurement geometry. Polarized light signals typically become unmeasurable after several millimetres of propagation in most tissues (~4–6 mm [68–70]) due to strong tissue scattering and depolarization effects. Generally speaking, transmission-type geometries are limited to thin tissue samples, whereas reflectance-based geometries are the only available configuration for bulk tissues. For the latter, it may be useful to determine the effective polarimetric sampling depth, for example through modelling and simulations [71, 72]. The other detection consideration is whether spatial polarimetric information is desired. If so, an *imaging* mode must be employed using a grid of photosensitive elements such as a CCD detector, otherwise, the light may be detected with a *point-sensor* (e.g. using a photodiode). Imaging may be preferable in many biomedical applications, however, it is slower than point-sensing and often challenging to perform while maintaining high SNR detection. In the case of the PEM, for example, its harmonic frequencies are synchronized with the intensity signal from a single photosensitive

element for high SNR synchronous detection, but major synchronization challenges arise when introducing a grid of imaging photodetectors.

On the information side, the major consideration is technique simplicity/complexity versus the resultant information content; the optimum compromise on this continuum is often task-specific, that is driven by the specific biological or clinical question to be addressed. In general, MM approaches are on the complex end of the polarimetry measurement/analysis spectrum, requiring at least 16 separate experimental polarization configurations to be recorded such that all elements of the MM can be derived. The benefit of this added complexity is that one obtains the complete polarization response of the interrogated material, and the resultant biophysical properties derived from MMs – for example retardance, optical rotation, diattenuation, and depolarization – are indicative of material biophysics only. This is in contrast with simpler polarimetric approaches such as crossed linear polarizers and various forms of Stokes polarimetry/ellipsometry, generally yielding fewer measured parameters that now depend on both material properties *and* (generally uninteresting) polarization optics of the measurement system. For each biomedical application then, one should consider the sufficiency of the obtained information content and whether the 'contamination' of results with experimental system details is acceptable. It is important to point out that measurement complexity considerations (and associated speed and cost) may become moot as technology advances to yield simpler/faster/cheaper MM measurements and analysis systems. We revisit these topics in the next section after reviewing various biomedical examples.

## 3 Biomedical Applications of Mueller Polarimetry

Many adverse physiological processes are associated with morphological and compositional changes in tissues which affect their polarization properties and enable polarimetric detection. Depolarization and linear retardance have found the most diagnostic use thus far since they are the strongest occurring bio-polarimetric effects due to the strong scattering effects of most tissues, along with the presence of birefringent fibrous structures. Diattenuation and dichroism appear much weaker and have not yet been of much biomedical use. Optical rotation (circular retardance) is also rather weak in biotissues due to modest concentrations of chiral molecules, but may eventually prove useful for non-invasive glucose monitoring of diabetic patients which remains one of the most important unsolved problems in clinical medicine [38, 73].

Polarimetric signals are cumulatively sampled over depth (as most polarimeters do not offer depth discrimination capabilities) and this complicates the interpretation of the resultant measurements in heterogeneous tissues (especially in the bulk-tissue reflectance geometry) [70]. The measurements may be further conflated when employing the abovementioned *non-Mueller* techniques due to their admixing of experimental parameters. MM polarimetry, with its ability to exclusively describe

sample properties and to decouple the 'lumped' polarization effects into their biophysically interpretable 'basis' properties, is thus beginning to demonstrate exciting and promising biomedical diagnostic capabilities. Heart infarctions, for example, cause significant remodelling of the myocardium, as do corresponding stem cell regenerative treatments, enabling both to be identified polarimetrically via Mueller retardance imaging [74]. Bladder obstruction can also be assessed through retardance imaging due to the induced strain on the bladder walls (strain birefringence) [35, 36]. But oncology has been the most actively explored medical field by the polarimetry community, driven by the importance of cancer detection/diagnosis/staging problems, and the prominent polarimetric changes due primarily to cellular and stromal (pre)malignant transformations associated with cancer development and growth [75–77]. In this section, we thus focus on detection and characterization of pre-cancer and cancer via several illustrative examples. A more complete list of polarimetry's presence in biomedicine can be found in the recently published comprehensive review [78].

## *3.1 Mueller Polarimetry and Pre-cancer/Cancer*

Pre-cancer-to-cancer progression is marked by well-known changes to cellular concentration (cellular proliferation) which affects light-scattering [65, 66] and hence depolarization [20, 79, 80], as well as changes to collagen organization which affects both linear birefringence [81, 82] and depolarization [83]. Polarimetric contrast can thus be generated between (pre)cancerous and non-cancerous tissues. Early Mueller polarimetry experiments in the 2000s demonstrated this and highlighted its potential for clinical use, such as the study by Smith et al. [31], which identified malignant moles and lupus lesions of skin in vivo via retardance and depolarization images. Similar work was performed by Chung et al. [84] which demonstrated polarimetric diagnosis of oral pre-cancers in hamster cheek pouches in vivo. Since then, there have been several studies in various configurations to investigate and advance MM diagnostics of pre-cancer and cancer.

**Mueller Imaging of Thin Tissues: Transmission-Based Configurations**
Although limited in clinical scope relative to bulk tissues studies, thin tissues enable more detailed polarimetric assessment through higher SNR signals (minimal scattering), the ability to section tissue to isolate regions of interest without depth interference and availability of correlative ground-truth histology [85]. Notably, the latter is actually expensive and often subjective and difficult to reproduce [86, 87]. Polarimetry may thus improve upon current methods with its label-free, cost-effective, and quantitative (objective) characteristics. An important transmission-based thin tissue study was performed by Shukla et al. [82] which investigated the polarization responses of epithelial and stromal tissue of cervical dysplasia (pre-cancer). As seen in Fig. 3, depolarization is sensitive to cellular dysplasia of the epithelium (top row) and retardance is sensitive to stromal changes (bottom

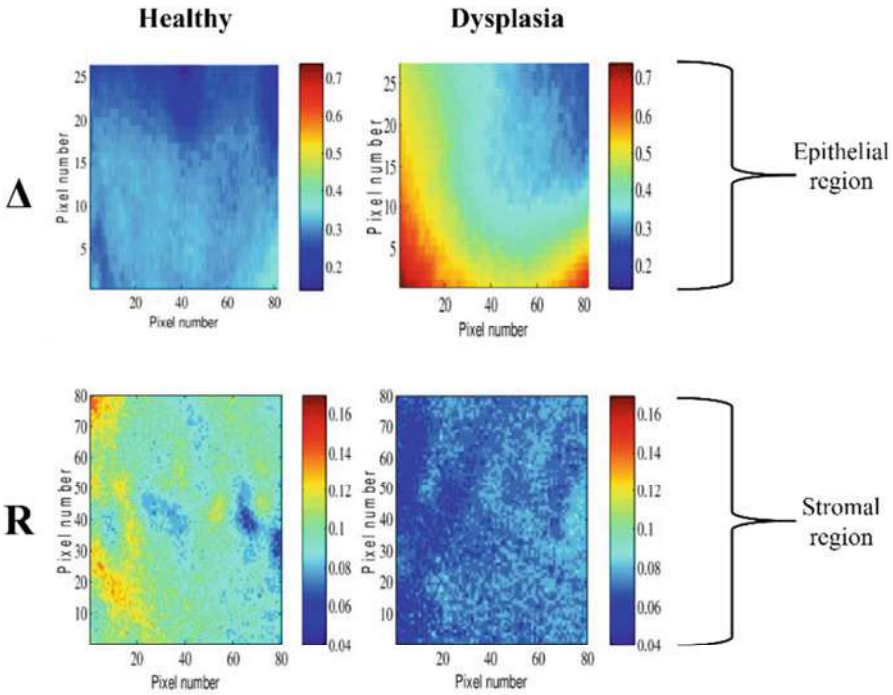


**Fig. 3** Depolarization images (Δ, top row) of healthy and dysplastic epithelium regions of cervical tissue; note the increasing depolarization in the latter. Corresponding retardance images (R, bottom row) of healthy and dysplastic tissues in the stromal regions of cervix; decreasing retardance in dysplastic stroma is clearly seen. The tissue dimensions were 4 mm × 6 mm and 5 μm thick. (Adapted from [82])

row). Since epithelia are typically devoid of fibrous (birefringent) structures, the depolarization contrast arises from the pleomorphic and proliferative alterations to cells which affect the scattering anisotropy (related to scatterer size) and scattering coefficient (essentially the *turbidity*, related to scatterer concentration). In the connective tissue compartment, healthy stroma exhibits strong birefringence due to the ordered structure of its well- aligned collagen fibres, which is diminished during precancerous remodelling of more chaotic collagen networks [81]. These distinct polarimetric microstructural biomarkers have recently been used to assess breast cancer tissue slides at different pathology stages [88]; these promising results necessitate further studies in this area towards establishing a polarimetric clinical niche.

**Mueller Imaging of Bulk Tissues Ex Vivo: Reflectance-Based Configurations**

In light of the useful MM polarimetric probing ability of (pre)cancers shown in thin tissues, there is a push towards its in-vivo diagnostics to offer an informative alternative to the invasive tissue biopsies currently employed for (pre)cancer detection.

In-vivo assessment of course involves bulk tissues which must be examined in the backscatter direction. Bulk tissues are much more challenging than thin tissues to assess polarimetrically, since (1) there is a major increase in depolarization yielding overall weaker signals, (2) backscattered polarized light responds differently and more complexly than forward scattered light (e.g. helicity flipping and multiple backscattering pathways) [21, 22, 89], and (3) depth-effects (e.g. tissue layers which exhibit different polarization responses [70]) are introduced which can lead to unexpected results. It is thus important to assess the feasibility of bulk tissue characterization ex vivo before introducing further challenges of in-vivo examination.

Pierangelo et al. [90] presented an interesting polarimetric assessment and potential staging of bulk tissue cervical cancers ex vivo. Here, the freshly excised cervical samples were imaged *en face* (i.e. stroma beneath the epithelium), in contrast with the Shukla study [82] which isolated the epithelia and stroma through thin-slice sectioning. Dysplastic lesions, referred to as Cervical Interepithelial Neoplasia (CIN), are staged as the malignant cells approach the surface of the epithelium; the progressive stages CIN1, CIN2, and CIN3 indicate when one-third, two-thirds, or the entire epithelium is transformed, respectively. These cervical dysplasia stages along with their affected regions can be identified by MM polarimetry, as shown in Fig. 4a. As seen, depolarization decreased from healthy to CIN1 to CIN3 to glandular tissue and retardance disappeared in the dysplastic stages. But in fact one would expect depolarization to behave oppositely, instead increasing in dysplastic regions due the higher cellular concentrations (resulting in higher turbidity) as previously observed [82] (see Fig. 3); bulk tissue and backscatter geometry effects are likely responsible. Novikova et al. [91] proposed that *increased* backscattered polarization preservation from cancerous tissue may stem from entrapment of multiply scattered depolarized light and increased absorption arising from the strong vascularization in the tumour region, with both of these mechanisms yielding higher DOP of the detected light as observed. Further investigation is needed, but nonetheless significant polarimetric contrast was observed. Also unexpected was the large decrease in retardance of dysplastic regions as epithelia is largely absent of birefringent tissue; the authors attributed this to connective tissue lying beneath the epithelium, since dysplasia has been found to disrupt the organization of neighbouring stroma [81, 82, 92]. Rehbinder et al. [93] then applied thresholding to the retardance images of cervical tissue samples to separate healthy (above the retardance threshold) from abnormal regions (pre-cancerous or cancerous, below the retardance threshold), as shown in Fig. 4b. These interesting MM polarimetric responses have shown their potential in diagnosing cervical pre-cancers; however, the bulk tissue retroreflection imaging geometry and the resultant depth-cumulative polarimetric sampling introduce curious effects. These effects may be elucidated by depth-resolved hybrid modalities which are discussed in Sect. 4.1.

**Mueller Imaging In Vivo**

The ex-vivo studies of both thin and bulk tissues show that the information content afforded by MM polarimetry is promising for assessing pre-cancerous

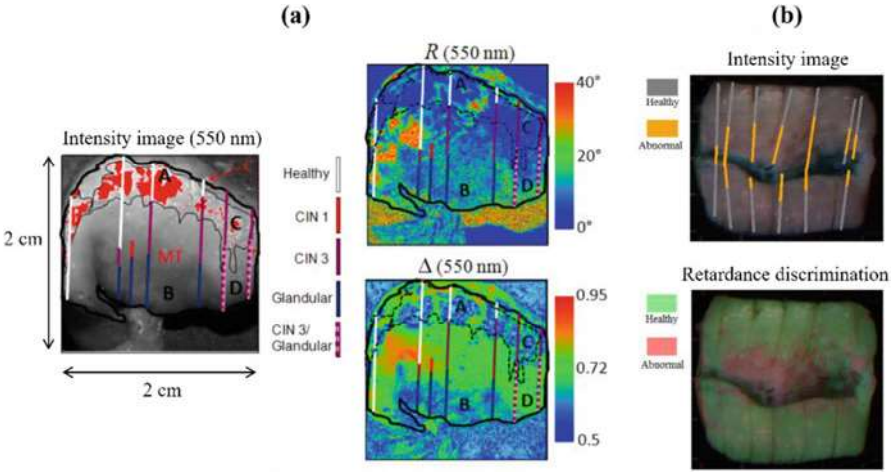


**Fig. 4** Polarimetric staging of cervical cancer pathology. (**a**) Intensity image of surgically excised human cervical specimen with overlayed histological characterizations denoted by coloured lines (see legend); histology was performed after polarimetric imaging. The interior of the black solid line is malpighian (squamous epithelium) denoted by 'MT' and the exterior is stroma denoted by 'C'. The thin solid line delineates a region where polarimetric data may be inaccurate and the red coloured areas indicate saturation of the CCD. Retardance R (*top*) and depolarization Δ (*bottom*) images of the specimen exhibiting healthy, CIN1, CIN3, glandular, and CIN3/glandular (glandular buried beneath CIN3 tissue) regions. Depolarization appears to exhibit promising staging capability where each stage (except for CIN3/glandular) is marked by different values (decreasing from healthy to CIN3). Retardance compliments the depolarization image with clearer identification of healthy zones (strong retardance) and slight identification of CIN3/glandular tissue. (Adapted from [90]). (**b**) Intensity image (*top*) of surgically excised human cervical specimen with overlayed histological characterization denoted by coloured lines (see legend). Applied to the intensity image, retardance (*bottom*) is used as a discriminating parameter where above-threshold values are coloured green to indicate healthy tissue and below-threshold values are untouched to indicate diseased tissue. Retardance appears to be sufficient in assessing cervical pre-cancer/cancer and in delineating pathological margins. (Adapted from [93])

and cancerous tissues. This has recently led to efforts towards in-vivo imaging with a focus on technology development to address various clinical engineering challenges. In-vivo Mueller polarimeters must be robust, rapid (to minimize motion artefacts), accurate, and ideally cost-effective to successfully function in realistic clinical conditions [94]. Several such studies have focused on in-vivo cervical (pre)cancer assessment to improve upon current screening methods. Currently, colposcopy (low magnification examination of the cervix) of high grade dysplasia only yields 60–70% sensitivity and 50% specificity [95]; there is also low inter-operator reproducibility ($\kappa = \sim 0.4$) [96], thus suggesting highly operator-dependent results. Towards this goal, Ramella-Roman's group [97, 98] recently demonstrated a portable hybrid colposcope in the form of a snapshot MM polarimeter (Fig. 5i). The PSG consisted of a set of light-emitting diodes to provide the three linear states (vertical, horizontal, 45°) and right circularly polarized light. The novel

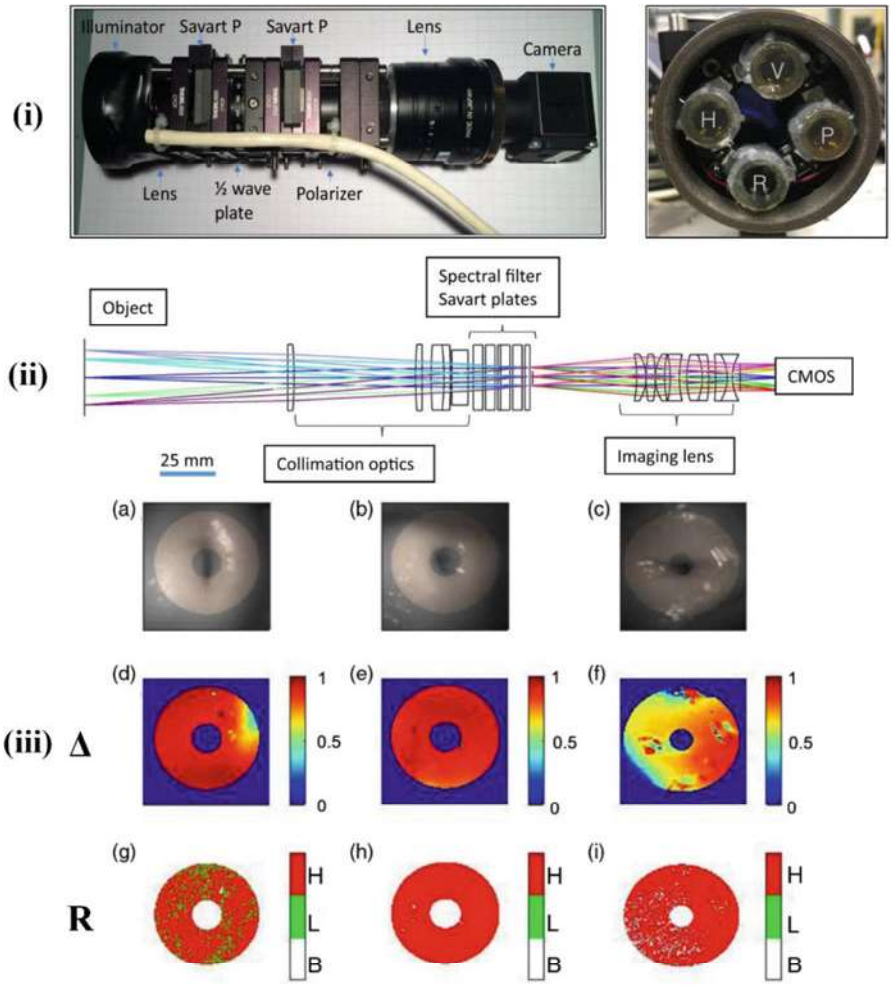


**Fig. 5** Portable colposcope 'Snapshot' MM polarimeter. (Figures from [98]). (**i**) The portable snapshot Mueller polarimeter shown on the left panel; the illuminator (PSG) output end is shown on the right. The compactness, speed, and lack of moving parts are attractive features for clinical adoption. (**ii**) Schematic of the PSA portion of the system. (**iii**) In-vivo images of three healthy cervices (field of view = 30 mm diam). (a)–(c): intensity images; (d)–(f): depolarization images; (g)–(i): retardance images with corresponding intensity bars, where H and L indicate high and low retardance (threshold at 25°) and B indicates zero background. The trend of high and high retardance of the healthy cervices agrees with previously reported data (whereas precancerous regions are associated with lower values of these two metrics [90]). The non-uniformity of the depolarization image in (f) may be due to the heterogeneity of the cervix

PSA comprised of a quarter wave retarder and linear polarizer on either side of four Savart plates which divided the incident light into four separate paths. An imaging lens recombined the four separate channels onto the camera to create a

spatial interference pattern, where the fringes are a modulated transfer function of the optical elements and the polarimetric properties of the illuminated sample. Either Fourier transform or so-called sliding reconstruction was used to recover the sample's polarization properties (Fig. 5ii). The total acquisition time was approximately 1 s, suitable for in-vivo measurements. Furthermore, the cost of the polarimeter was estimated to be a modest ~$200 USD, a significant reduction compared to the typical cost of current colposcopes (~$2000 USD), and the system was fully powered by a laptop computer, eliminating the need for electrical outlets. Both of these practical advantages may enable wider deployment in lower resource settings.

In-vivo images were acquired of healthy cervices, three of which are shown in Fig. 5iii in the form of raw intensity, depolarization, and retardance images (the latter two derived from polar decomposition of the measured MM). The depolarization and retardance results were in agreement with previously reported data on healthy uterine cervices. One patient had a polyp that was marked by lower depolarization (data not shown), also in agreement with previous observations [95]. The imaging results of healthy cervical tissue are thus in line with the literature; the next step will be to validate the imaging accuracy in pre-cancerous and cancerous tissues. Overall then, this study demonstrates the feasibility of in-vivo cervical Mueller imaging in a clinical setting, using a cost-effective and easy-to-employ (laptop powered) polarimeter to enhance its clinical adoptability.

Another promising approach for in-vivo assessment of uterine cervix pathology is that by Vizet et al. [95] who mounted a miniaturized Mueller polarimetric imager onto a conventional colposcope (a stereoscopic binocular microscope used to illuminate and observe uterine cervix under low magnification of ~4–6X). This approach exploits the powerful advantage of Mueller polarimeters (and of most polarimetric systems in general), in that they are highly compatible with existing photonic devices so they may be rather simply placed in a beam path to furnish additional polarimetric information. The silica fibre bundle used for light delivery in the colposcope was replaced by a liquid light guide to increase the illumination intensity and ensure a measurable backscattered signal. The mounted polarimeter was sealed within an airtight metallic box measuring $3 \times 5 \times 10$ cm$^3$ that could be toggled between 'OFF' or 'ON' to enable regular colposcopic or MM imaging. The PSA of the Mueller polarimeter consisted of a linear polarizer followed by two tuneable ferroelectric liquid crystal cells that sandwiched a quarter wave plate: the PSG was the reverse order version of these elements and the CCD camera detected 550 nm light using a bandpass dichroic filter. The polarimeter was capable of acquiring a single polarization configuration image in 100 ms, resulting in a full MM (16 images) acquisition time of 1.6 s, suitable for in vivo imaging to reduce patient motion artefacts.

Before in-vivo imaging, the performance of the polarimetric colposcope was tested on ex-vivo cervical specimens, which compared the novel rapid 1.6 s acquisition Mueller images to (1) averaged Mueller images acquired over ~25 s (16 images) and (2) Mueller images from a previously demonstrated and routinely used Mueller polarimeter [47, 90]. Reasonable agreement between the three methods was

demonstrated. The thus-validated 1.6 s Mueller polarimeter was then used to image healthy uterine cervices in vivo (single images, not averaged), one of which also contained a polyp. The polyp served as a test case for tissue structure distinct from normal healthy epithelium, approximating a pathological (pre-cancerous/cancerous) lesion; polyps are layered with glandular (columnar) epithelium, whereas the exocervix is layered with Malpighian (squamous) epithelium. The healthy Malpighian tissue exhibits high retardance as expected due to its well-ordered collagen, whereas the polyp is well delineated by its very low retardance. Additionally, the polyp appears to be less depolarizing compared to the exocervix. The polarimeter is thus capable of discriminating between glandular and squamous tissue types, demonstrating its potential for pre-cancer/cancer detection of cervices. Moreover, this was performed using a validated, robust, rapid, and accurate in-vivo Mueller imaging tool, which was easily operated by the surgeon as reported. As in the previous example, the next step in using the device will be to image cervical pre-cancers and cancers to determine the polarimetric discrimination capabilities at such rapid speed in practical situations, particularly to determine the feasibility of differentiating between polyps and pre-cancerous lesions which both seem to exhibit low retardance and low depolarization.

**Section 2.5 Revisited: Is the Full Mueller Matrix Approach Really Necessary?** For all its advantages, Mueller polarimetry is a rather complex technique that requires several measurements (at least 16) and often relies on advanced technologies to enable practical and robust systems. As touched upon in Sect. 2.5, an important question then arises: Are Mueller matrices really worth measuring? Can adequate polarimetric information be attained in a simpler manner? Indeed, the added complexity of the Mueller approach, despite furnishing its associated rich information content, may not be necessary in all applications, and simpler polarimeters have thus been proposed and demonstrated. For example, Jacques et al. [83, 99] and Backman and Gurjar et al. [65, 66] have employed simple cross-linear and co-linear polarizer setups to differentiate between superficially scattered and deeper penetrating polarized light in epithelial tissues based on light depolarization rates. DOP depth discrimination using rotating polarizers and retarders has also been recently reported by Da Silva et al. [71, 72, 100–103] for probing epithelia using the *ellipticity* of light. Stokes DOP approaches have been applied to skin cancer detection and characterization with promising early results [104, 105], as well as towards carcinomas of the lung [106] and colon [107, 108]. Tissue birefringence has also been studied in the recent works of Vitkin et al. [109–111] which used simple rotating crossed polarizers to characterize morphological stromal features of human breast cancer slides.

Such simpler approaches – crossed- and co-linear polarizers and Stokes polarimeters – have primarily found applications in tissues where *only* depolarization or retardance is sufficient for characterization (e.g. epithelia contain little birefringent materials, leading to non-Mueller successes via DOP-based measurements). MM polarimetry, with its multiple polarization measurement configurations and matrix interpretation/decomposition analysis, is likely an

'overkill' if only one polarimetric response is satisfactory. The success of these non-Mueller approaches on epithelia can also be attributed, at least in part, to Mie theory [112] which has played a significant role in the understanding of the light scattering physics in such media where cell nuclei can be modelled as discrete scattering particles, having facilitated the use of microsphere suspensions as tissue phantoms and Monte Carlo computer modelling of polarized light propagation in turbid materials [21–23]. Indeed, one of the first proposals for depth discrimination using polarized light [24] relied on both of these tools.

However, many tissues, particularly those in bulk form, are both turbid and birefringent (as well as possibly optically active, linearly/circularly dichroic, and other second-order effects), which plays to the strengths of MM polarimetry since these can be retrieved and decoupled via decomposition and all used for pathological assessment as clearly demonstrated in preceding illustrations. An interesting case in point was recently provided by Pierangelo et al. [90] who attempted to analyse cervical dysplasia using orthogonal state contrast (OSC) imaging (DOP information) which showed some discrimination between the two tissue types. However, as the authors remarked, 'OSC imaging is not adequate for such samples, as it does not provide enough information to extract the relevant polarimetric parameters for healthy and anomalous tissues. To properly characterize the polarimetric response of healthy and pathological cervical tissue, full Mueller polarimetry is clearly needed'. Another example is the Stokes-DOP-based study by Anastasiadou et al. [107] which showed detection capability of cervical cancer and some visualization of margins, however to a far weaker extent than that shown by the MM depolarization and retardance images of Shukla et al. [82]. Moreover, the attractive simplicity of non-Mueller approaches may become a less important design consideration since technological advances are enabling easier acquisition of Mueller matrices through automation such as the snapshot polarimeter by Ramella-Roman et al. [98] and the ferroelectric liquid crystal cell-based polarimeter by Vizet et al. [95]. Therefore, with the advent of new instruments and approaches to measure MMs and faster computers to more rapidly analyse/decompose them for useful biomarker extraction, the use of this 'more complete' variant of polarimetry may prove readily feasible, and thus more widespread. Indeed, biomedical technologies tend to develop by clinical necessity driven by a biomedical pull: if an application calls for better instruments, engineers promptly take on the challenge. Such has been the story of MM polarimetry as an emerging technique in biomedicine.

## *3.2 Probing Sub-Micron Structural Anisotropy for Pre-cancer Detection*

Probing the tissue structural anisotropy through MM measurements have been promising, however there is still much room for improvements, for example if the spatial sensitivity of the polarimetric techniques is improved down to the scale of

*microscopic anisotropy* of tissue architecture (micron/sub-micron length scales). It has been suggested that pre-cancer involves altered interactions between superficial epithelial cells and the underlying connective tissue, and the resulting changes in the *anisotropic* connective tissue morphology are rather subtle. These typically manifest optically as small changes at the sub-micron scale. Indeed, initial findings on sub-micron scale anisotropy in tissue multifractality derived from spectral Mueller matrices have shown that *microscopic* refractive index asymmetries are a much better metric of subtle pre-malignant transformation [113, 114] compared to the 'conventional macroscopic' polarimetry biomarkers discussed earlier. Here, a brief account of this promising research direction is provided.

Multifractals are a special class of complex self-similar processes, observed in diverse natural systems encompassing biology, material structures, physiological time series, turbulence, etc. [115–118]. Such complex signals typically consist of many interwoven fractal (self-similar) subsets, each of which are characterized by their own local scaling exponents (known as Hurst exponent, $0 < H < 1$) [115, 119]. Initial findings on tissue multifractality were based on *forward* multi-resolution analysis of differential interference contrast images of tissue [92] and *inverse* analysis on tissue light scattering spectra [120]. A state-of-the-art algorithm for multifractal research, the multifractal detrended fluctuation analysis (MFDFA), was optimized to extract and quantify the tissue multifractal parameters, namely, the generalized Hurst exponent ($h(q)$, $q$ is the order of the moment) and the width of the singularity spectrum ($f(\alpha)$, $\alpha$ is the singularity strength) [119]. Interestingly, it was observed that the spatial refractive index fluctuations of tissue exhibit *microscopic* multifractal anisotropy that manifests as an intriguing wavelength-dependent linear diattenuation effect in the scattering Mueller matrix elements [113, 114]. The corresponding inverse problem was also addressed of extracting information on the microscopic multifractal anisotropy from the scattering Mueller matrix. This analysis is based on processing the wavelength dependence of selected Mueller matrix elements (that encode the diattenuation effect) in the Fourier domain using Born approximation followed by multifractal analysis. The model was applied on ex-vivo tissues of human cervix of different pathology grades. The experimental system of Fig. 2 was employed to record backscattering spectroscopic Mueller matrices for these studies, and the results are summarized below.

For the inverse analysis, it was identified that the multifractal anisotropy manifests most prominently in the wavelength variation of the $M_{12}(\lambda)$ and $M_{13}(\lambda)$ elements [113, 121] as these carry information on spectral linear diattenuation effect ($d(\lambda) = \frac{\sqrt{{M_{12}}^2+{M_{13}}^2}}{M_{11}}$). The spectral variations of these elements were analysed to extract information on the refractive index in homogeneity distributions along two orthogonal linear polarization directions ($\eta_{\parallel/\perp}(\rho)$ with $\rho$ being the length scale) through Fourier domain analysis using the Born approximation as [113].

$$\begin{aligned}\eta_{\parallel/\perp}(\rho) &\sim \int k^{-2}\left\{M_{11}(K) \pm \sqrt{{M_{12}}^2(K) + {M_{13}}^2(\beta K)}\right\}^{\frac{1}{2}} e^{-i(\mathbf{K}\ldots\boldsymbol{r})} d^3\beta \\ &= \int \left|s_{2/1}(K = 2\pi\nu)\right| e^{-i(\mathbf{K}\ldots\boldsymbol{r})} d^3\beta\end{aligned} \tag{13}$$

Here, $\boldsymbol{K}$ is the scattering vector with modulus $K = 2k\ \sin\left(\frac{\theta}{2}\right) = 2\pi\nu$, $\nu$ is the spatial frequency, $k = 2\pi/\lambda$ is the wave vector, $\lambda$ and $\theta$ are the wavelength and the scattering angle, and $s_{2/1}$ are the scattered field amplitudes for the two orthogonal polarizations. The extracted $\eta_{\parallel/\perp}(\rho)$ were then analysed via MFDFA to quantify the multifractal anisotropy parameters.

MFDFA is an advanced statistical tool for multifractal analysis as described in detail elsewhere [119]. Using this approach, any multifractal signal can be characterized via two sets of scaling exponents: (i) the generalized Hurst exponent $h(q)$ and (ii) the classical multifractal scaling exponent $\tau(q)$ along with the singularity spectrum $f(\alpha)$ [119]. These are inter-related as

$$\tau(q) = qh(q) - 1, \tag{14}$$

$$\alpha = \frac{d\tau}{dq}, \quad f(\alpha) = q\alpha - \tau q, \tag{15}$$

where $\alpha$ is the singularity strength and $\sigma$ is the full width of $f(\alpha)$ is a quantitative measure of multifractality. In monofractal approximation, the generalized Hurst exponent $h(q = 2)$ is equivalent to fractal dimension. The variation of $h(q)$ or $\tau(q)$ for other values of q indicates multifractality or multi-resolutions (different $q$ values) fractal dimension. The refractive index asymmetry distributions for orthogonal linear polarizations, $\eta_{\parallel}(\rho)$ and $\eta_{\perp}(\rho)$ were analysed separately using the MFDFA. The multifractal anisotropy was quantified via the differential classical scaling exponent, $\Delta\tau = |\tau(q = 2)_{\parallel} - \tau(q = 2)_{\perp}|$, and differential width of singularity spectrum $\Delta\sigma = |\sigma_{\parallel} - \sigma_{\perp}|$ for orthogonal linear polarizations.

With the theoretical context thus provided, Fig. 6 demonstrates multifractal anisotropy in the spectral Mueller matrix elements recorded from the connective tissue region of a Grade 1 pre-cancerous cervical tissue [113]. The $M_{12}$ ($\lambda$) and $M_{13}$ ($\lambda$) elements (Fig. 6a) and the resulting linear diattenuation parameter $d(\lambda)$ (Fig. 6b) exhibit considerable magnitude and wavelength variation (overall decay with $\lambda$), a potential signature of fractal (multifractal) anisotropy. This is characteristically manifested as a power law dependence of the $|s_1(\nu)|^2$ and $|s_2(\nu)|^2$ light-scattering parameters (Fig. 6c) which were fitted with fractal power law ($|s_2(\nu)|^2 \approx \nu^{-(2H_{\parallel}+D_E)}$ and $|s_1(\nu)|^2 \approx \nu^{-(2H_{\perp}+D_E)}$). Here, $H_{\parallel/\perp} \in (0,1)$ are the Hurst scaling exponents and $D_E = 3$ is the Euclidean dimension of the scattering object. The fitting yielded multiple power law exponents at different $\nu$-ranges, suggesting multifractality. Importantly, fitting over broad $\nu$-range yielded differences in average Hurst exponents: $H = 0.55$ and $0.65$ derived from $|s_2(\nu)|^2$ and $|s_1(\nu)|^2$, respectively ($\Delta H = 0.1$). These results suggest self-similarity anisotropy in spatial refractive index variations.

Figure 6d and e summarizes the results of the more detailed multifractal analysis. Significant magnitudes of the differential classical multifractal scaling exponent [$\Delta\tau = |\tau(q = 2)_{\parallel} - \tau(q = 2)_{\perp}| = 0.16$] and differential width of singularity spectrum [$\Delta\sigma = |\sigma_{\parallel} - \sigma_{\perp}| = 0.85$] provided conclusive evidence of multifractal

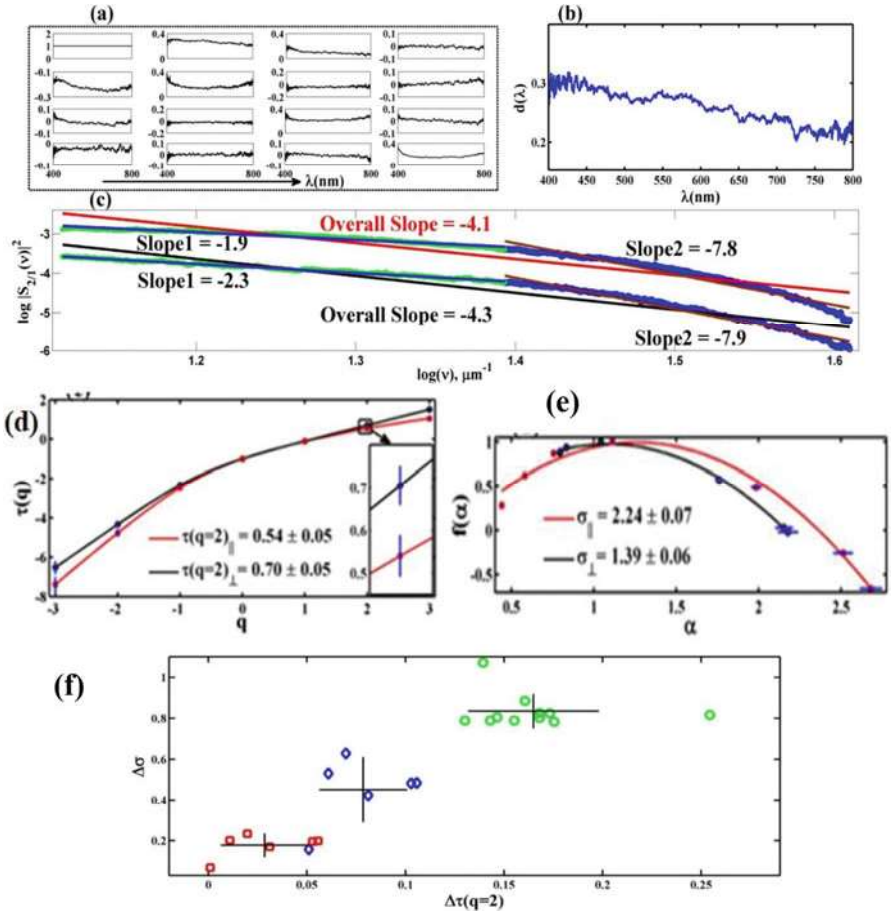


**Fig. 6** Manifestation of multifractal anisotropy in the wavelength variation of scattering Mueller matrix elements of a Grade I precancerous tissue. Wavelength variation of (**a**) the normalized Mueller matrix elements and (**b**) linear diattenuation parameter $d(\lambda)$. (**c**) The spatial frequency ($\nu$) distribution of the Mueller matrix-derived parameters $|s_2(\nu)|^2$ and $|s_1(\nu)|^2$ (log-log plot) via Eq. (13). Fitting at two selected $\nu$-ranges (lower [blue] and higher [brown]) and overall fitting (red for $|s_2(\nu)|^2$ and black for $|s_1(\nu)|^2$) are shown and the corresponding values for the slopes are noted. (**d**) The moment ($q$)-dependence of the classical multifractal scaling exponent $\tau(q)$ (inset highlights the anisotropy or difference in $\tau$ around $q = 2$) and (**e**) the corresponding singularity spectra $f(\alpha)$ derived from $\eta_{\parallel}(\rho)$ (red square) and $\eta_{\perp}(\rho)$ (black circle). The values for $\tau(q = 2)$ and $\sigma$ are noted. In (d) and (e) lines are guide for eye and the error bars represent standard deviations of the parameters for measurements on 10 non-overlapping spots. (**f**) The three different precancerous grades (Grade I – green circle, II – blue diamond and III – red square) are mapped by their differential classical multifractal scaling exponent, $\Delta\tau = |\tau(q = 2)_{\parallel} - \tau(q = 2)_{\perp}|$ and differential width of singularity spectrum $\Delta\sigma = |\sigma_{\parallel} - \sigma_{\perp}|$ for orthogonal linear polarizations. Higher grades of pre-cancers are associated with decrease of both $\Delta h$ and $\Delta\sigma$ parameters, nicely separating different pathologies and implying reduction in multifractal anisotropy. (Adapted from [113])

anisotropy. Most importantly in the biomedical context, the values of $\Delta\tau(q=2)$ and $\Delta\sigma$ (1) cluster and (2) are observed to decrease with increasing pathology grades (Fig. 6f), suggesting a reduction in the multifractal anisotropy. This decrease in multifractal anisotropy was attributed to the disorganization of locally anisotropic microscopic domains (the collagen molecules and micro-fibrils) and/or reduction in local microscopic birefringence with increasing pathology grades [113, 121]. Importantly, none of the above trends could be gleaned from Mueller matrix-derived *macroscopic* linear retardance R $\delta$ parameters, which were generally low and did not exhibit appreciable difference between different grades (corresponding birefringence values at 600 nm were $0.08 \pm 0.03$, $0.04 \pm 0.02$ and $0.09 \pm 0.05$ rad for Grades I, II and III tissues, respectively; thus, no inter-grade separation was evident). These results suggest that the *microscopic* refractive index asymmetries are more sensitive to subtle pre-malignant transformation [113, 114, 121–123], as also often posited in the literature.

### 3.3 *Fluorescence Mueller Polarimetry: A Spectroscopic Diagnostic Tool*

Most biomedical polarimetry studies examine elastically scattered light from tissue that mainly carries morphological information. Conversely, polarization properties of fluorescence may provide valuable biochemical information on the changes in chemical structure, molecular organization, and local environment of the tissue fluorophores. However, the fluorescence polarization anisotropy parameter [124] traditionally measured reflects 'lumped' effects and is dominated by fluorescence depolarization in addition to the 'true' *intrinsic* tissue anisotropy that originate from the anisotropic molecular orientation and organization. Hence, a more encompassing fluorescence MM polarimetric approach has recently been developed [125, 126]. One can then polarimetrically probe and quantify the molecular orientation and organization of endogenous tissue fluorophores using this approach. The experimental system shown in Fig. 2 was employed to record fluorescence spectroscopic Mueller matrices ($\lambda_{ex} = 405$ nm, $\lambda_{em} = 450 - 750$ nm) in the exact backscattering configuration from connective tissue regions of precancerous human cervical tissues of different pathology grades [126–129]. These were then subjected to inverse analysis to yield the *intrinsic* fluorescence anisotropy parameters, namely fluorescence spectral diattenuation (differential excitation of fluorescence by orthogonal polarizations) and fluorescence polarizance (differential emission of fluorescence by orthogonal polarizations).

The analysis is based on writing the fluorescence Mueller matrix $\mathbf{R}$ as the product of three matrices such that $\mathbf{R} = \mathbf{M_1} \cdot \mathbf{M_d} \cdot \mathbf{M_0}$. Here, the matrix $\mathbf{M_d}$ is the dipole scattering Mueller matrix which takes care of the depolarization effects (both intrinsic and extrinsic) associated with fluorescence emission [125, 126]. The other two matrices $\mathbf{M_0}$ and $\mathbf{M_1}$ account for the absorption anisotropy of the ground molecular state (representing differential excitation of fluorescence with orthogonal

polarization) and emission anisotropy of the excited molecular state (representing differential emission of orthogonally polarized light), respectively. Using standard form of these matrices and with appropriate approximations [125, 126], it can be shown that the elements $R_{12}$, $R_{13}$, $R_{14}$ (first row of fluorescence Mueller matrix) encode excitation anisotropy of the ground molecular state and $R_{21}$, $R_{31}$, $R_{41}$ (first column) reflect emission anisotropy of the excited molecular state (cf. discussion following Eq. (9)). The intrinsic anisotropy effects of fluorescence are subsequently parameterized and quantified via the fluorescence diattenuation and polarizance parameters as [125, 126, 130]

$$\alpha_T = \frac{\sqrt{R_{12}^2 + R_{13}^2 + R_{14}^2}}{R_{11}}, \qquad \alpha_L = \frac{\sqrt{R_{12}^2 + R_{13}^2}}{R_{11}}, \qquad \alpha_C = \frac{R_{14}}{R_{11}}, \tag{16}$$

$$\beta_T = \frac{\sqrt{R_{21}^2 + R_{31}^2 + R_{41}^2}}{R_{11}}, \qquad \beta_L = \frac{\sqrt{R_{21}^2 + R_{31}^2}}{R_{11}}, \qquad \beta_C = \frac{R_{41}}{R_{11}} \tag{17}$$

where $\alpha_T$, $\alpha_L$, and $\alpha_C$ are the total, linear, and circular fluorescence diattenuations, respectively, $\beta_T$, $\beta_L$, and $\beta_C$ are the total, linear, and circular polarizance, respectively.

Figure 7 shows typical fluorescence Mueller matrix $\mathbf{R}(\boldsymbol{\lambda})$ recorded from the connective tissue (stroma) region of a dysplasia grade III pre-cancerous cervical tissue [130]. The fluorescence spectra peaking around 500 nm with 405 nm excitation is primarily contributed by fluorescence from collagen and other endogenous tissue fluorophores elastin and NADH. While strong depolarization of fluorescence is evident from the small magnitudes of the diagonal elements ($R_{22}$, $R_{33}$, $R_{44}$), relatively higher magnitudes of $R_{12}$ and $R_{21}$ elements indicated the presence of strong excitation and emission (respectively) *intrinsic* anisotropies of fluorescence. The corresponding fluorescence linear diattenuation (excitation anisotropy – $\alpha_L$) and fluorescence linear polarizance (emission anisotropy – $\beta_L$) parameters from typical grade I and grade III tissues samples showed significant magnitudes and prominent differences (Fig. 7b and c). The origin of these intrinsic linear anisotropies of fluorescence was linked to the crossed-linked collagen molecular structure in the connective tissue [130]. The rather weak but non-zero circular anisotropies ($\alpha_C$ and $\beta_C$) arises due to the presence of chiral moiety or helical molecular organization in the collagen structure. The reduction in the $\alpha_L$ and $\beta_L$ anisotropy parameters in grade III tissue was attributed to the destruction of the collagen cross-links and the resulting loss of intrinsic linear anisotropic organization in the collagen molecular structure. These results suggest the sensitivity of the fluorescence Mueller polarimetry towards changes in the intrinsic molecular organization and orientation of tissue fluorophores. The actual potential of these intrinsic fluorescence anisotropy parameters as biomarkers for pre-cancer detection remains to be rigorously evaluated.

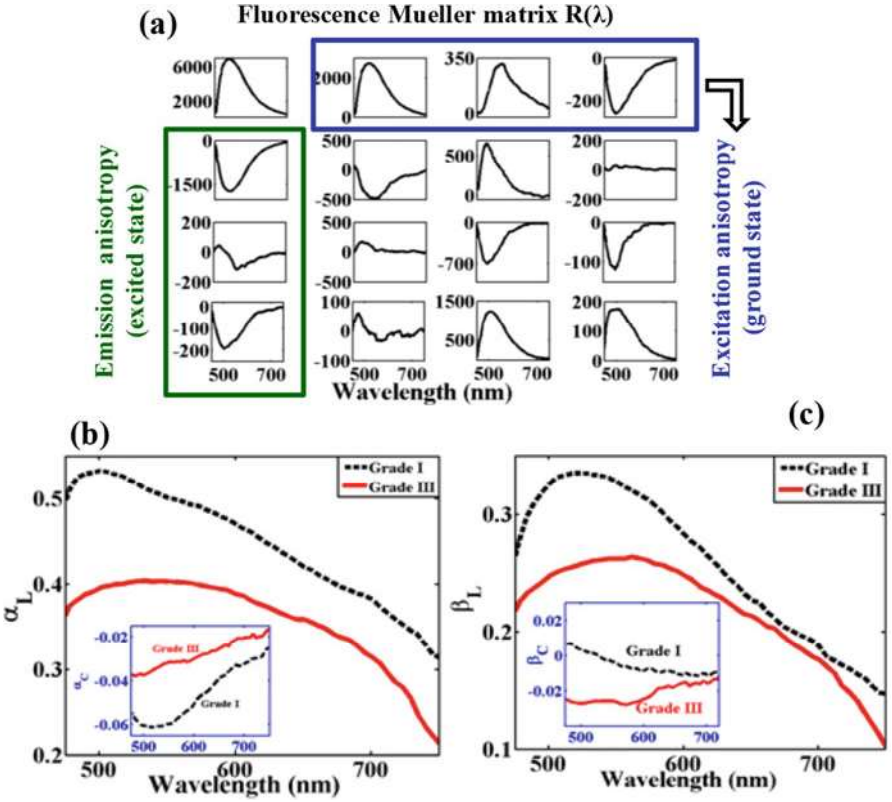


**Fig. 7** (**a**) Typical fluorescence spectroscopic Mueller matrix **R** ($\lambda_{em}$ = 450–750 nm) recorded with $\lambda_{ex}$ = 405 nm excitation from the connective tissue region of a dysplasia grade III precancerous cervix. The first element ($R_{11}$) represents the polarization-independent fluorescence spectra. The other three elements in the first row (blue) represent excitation anisotropy related to the ground molecular state; the three elements in the first column (green) represent emission anisotropy related to the excited molecular state. The spectral variation of (**b**) fluorescence linear diattenuation ($\alpha_L$) and (**c**) fluorescence linear polarizance ($\beta_L$) parameters for typical grade I and grade III precancerous cervical tissues. The insets show the variation of fluorescence circular diattenuation ($\alpha_C$) and circular polarizance ($\beta_C$) for the same tissues. (Adapted from [130])

## 4 Hybrid and Endoscopic Mueller Approaches

### *4.1 Depth-Resolved Hybrid Modalities: Elucidating Depth Effects*

Most tissues are heterogeneous throughout, where certain sub-regions may exhibit different polarization responses [70]. Since MM systems are typically not depth-resolved but instead gather tissue polarimetric information throughout their entire sampling depth, ambiguous and unexpected effects can arise (e.g. findings of

Pierangelo et al. [90] discussed above). It can therefore become important to elucidate depth effects; for example, this may help in differentiating tissue regions that exhibit similar depth-cumulative polarimetric responses such as in the aforementioned case of polyps and dysplastic lesions of cervix [95]. There has thus been an interest in combining/integrating Mueller polarimeters with depth-resolved modalities. Mueller polarimeters are advantageous in this regard due to their ease-of-integration with existing optical systems (e.g. the above-discussed colposcopic study by Vizet et al. [95]). OCT and confocal microscopy both offer depth-resolved imaging, thus prompting the polarimetry community to combine or integrate these technologies with Mueller polarimeters.

**Optical Coherence Tomography Combined with Mueller Polarimetry**

Optical coherence tomography (OCT) is a well-established depth-resolved tomographic imaging method [131, 132] routinely employed for in-vivo imaging; polarization-sensitive OCT (PS-OCT) has also been investigated for decades (for a detailed review see [133]). The time domain version of PS-OCT was first developed by Hee et al. [134], followed by the more sensitive, and thus more widely adopted frequency-domain versions (swept source and spectral-domain) [135]. PS-OCT relies on Jones vectors which describe fully polarized light interactions, and thus material depolarization cannot be determined. Instead, a parameter known as 'degree of polarization uniformity' (DOPU) [136] is invoked: the polarization state of each *speckle* is taken as unity (totally polarized), however in the case of a depolarizing medium, the polarization states of multiple speckles become randomized and uncorrelated, giving rise to the DOPU parameter. Mueller polarimeters may thus compliment PS-OCT systems by measuring actual material depolarization, and further PS-OCT systems can in return compliment Mueller polarimeters by providing information on axial tissue heterogeneity. To form this hybrid and complimentary imager, Chue-Sang et al. [51] have demonstrated a co-registration technique using a relatively simple PS-OCT system based on free-space optics and a Mueller polarimeter in a separate beam path. This enabled Mueller identification of burned regions of bovine tendon through diattenuation and depolarization images, as well as structural depth information of the bovine tendon via PS-OCT, shown in Fig. 8. This complimentary hybrid modality may be useful, for example, in identifying skin tumours through Mueller imaging, followed by assessment of their depth-of-invasion through PS-OCT imaging which can be an important prognostic factor [137, 138]. Furthermore, this approach may lead to better models for the recovery of local retardation using OCT-based imaging, rather than cumulative retardation [70], since many current recovery models rely on the measurement of surface retardance as a starting point [139].

**Second Harmonic Generation Confocal Microscope and Mueller Polarimeter Hybrid**

Instead of placing a Mueller polarimeter in a separate beam path as in the preceding Mueller-OCT co-registration example, it may be possible instead to integrate it directly in the beam path of a depth-resolved modality to furnish 3D

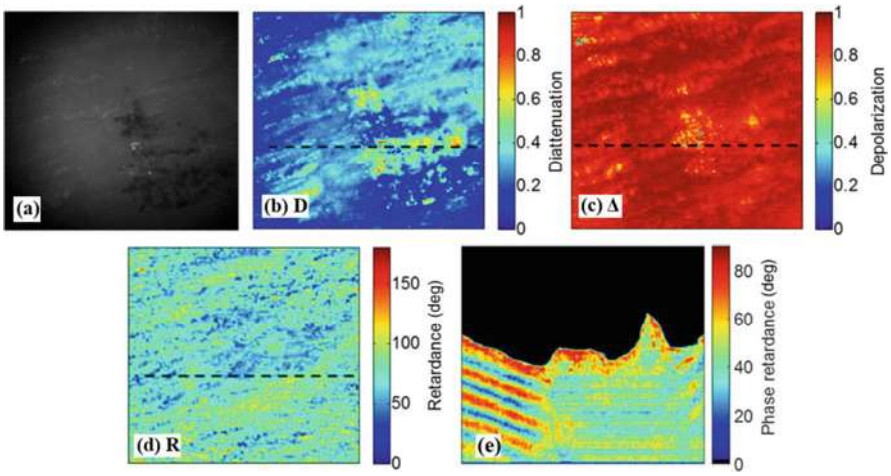


**Fig. 8** Mueller matrix imaging and polarization-sensitive OCT of bovine tendon with a burned region (tendon dimensions $4 \times 4 \times 2$ mm$^3$). (**a**) CCD image showing the burned region (darker parts at the centre to bottom right portion of the image). (**b–d**) show diattenuation, depolarization, and retardance images acquired by the Mueller polarimeter. The diattenuation image appears to best demarcate the burned region. (**e**) PS-OCT B-scan of tendon (at the location of the horizontal line in the *en face* MM images of (**b**)–(**d**)), showing the burn boundary well delineated by its low retardance due to the thermal disruption of the stromal organization. The region to the left exhibits an oscillatory phase retardance consistent with healthy tendon. Using such complimentary information from each modality may be useful, for example, in identifying skin tumours through Mueller polarimetry and then assessing their depth of invasion through PS-OCT which can be an important prognostic factor [137, 138]

depth-resolved Mueller polarimetric volumes. This may be done by hybridizing a confocal microscope with a Mueller polarimeter. Confocal microscopy performs optical depth sectioning using a pinhole at a confocal plane to beam focus at the sample, thus eliminating backscattered photons from out-of-focus sample depths which cause blurring. This combined modality may be further enhanced with the integration of non-linear microscopy to form a second harmonic generation (SHG) confocal MM microscope. SHG microscopy is an excellent method for imaging collagenous tissue due to its preferential SHG response [140] which can thus provide additional corroborative information alongside Mueller decomposed images to better understand the polarization response of tissue, as shown in Fig. 9a for benign and malignant breast tissues [141]. Through depth-scanning, a 3D MM polarimetric volume may be generated alongside associated SHG images at various depths, such as in the approach by Satyashev et al. [142] with corresponding results shown in Fig. 9b. This type of hybrid Mueller microscopy approach may indeed prove useful in gaining true depth-resolved polarimetric insight or assisting histopathological diagnosis. However, long acquisition times (on the order of tens of minutes at best) currently hinder its use beyond the laboratory.

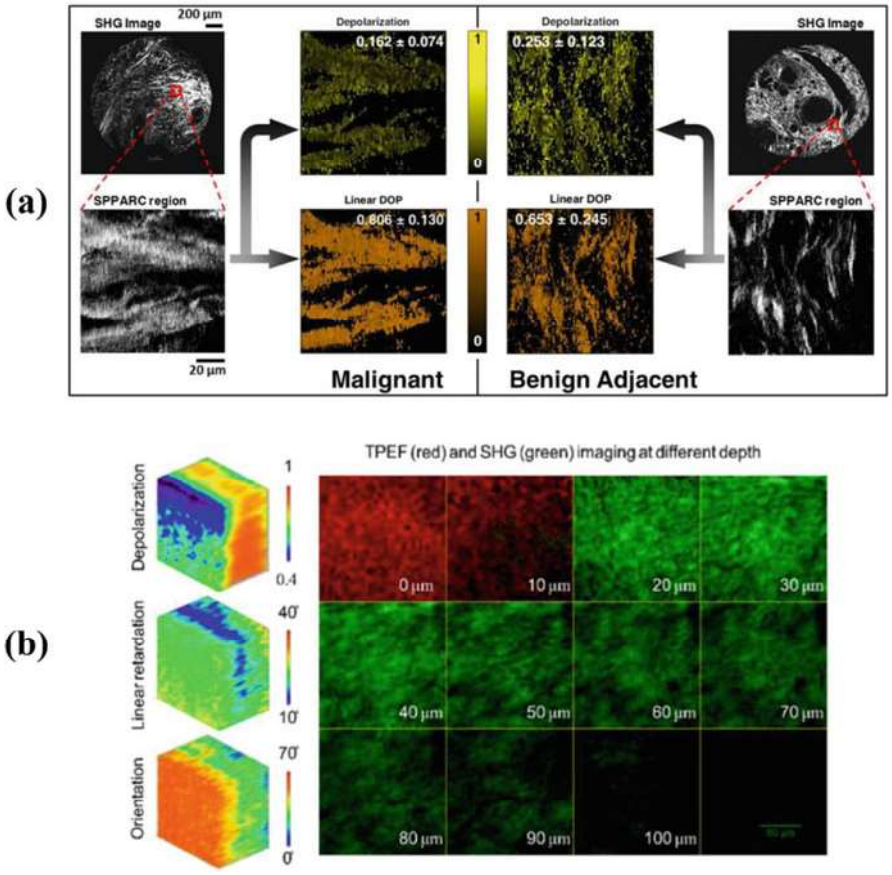


**Fig. 9** SHG confocal Mueller matrix microscopy. (**a**) The images on the left and right sides correspond to malignant and benign breast tissues, respectively. SHG microscopic images are shown on the top left and top right. Shown as insets below the SHG images are 'second-harmonic patterned polarization-analysed reflection confocal microscopy' (SPPARC) images of selected regions. Corresponding to the SPPARC images are depolarization and linear degree of polarization spatial maps (see arrows) (along with inset values indicating the mean and standard deviation over all pixels in each image). This technique enables high resolution polarimetric images of tissue samples to analyse microstructural differences between tissue types and their corresponding polarimetric responses. (Adapted from [141]). (**b**) Full-depth two-photon and Mueller matrix confocal imaging of rat cornea (field of view: 120 × 120 $\mu m^2$). The 3D polarimetric volumes on the left show depth-resolved determination of polarization responses in tissue which are generated by acquiring Mueller images confocally at incremental depths and then producing a 3D volume. This may help in differentiating between tissues which exhibit similar depth-unresolved cumulative polarimetric responses. The green SHG images on the right side can corroborate the Mueller decomposition images by providing information on collagen presence to assist in pathological detection. Two-photon excitation fluorescence was also imaged (TPEF, first two red panels in top row). (Adapted from [142])

### *4.2 Mueller Polarimetry as a Guidance Tool for Mass Spectrometry*

Mass spectrometry is a very accurate technique for characterizing the chemical composition of materials, including biological tissues, by analysing the mass-to-charge ratios of constituent ionized molecules and atoms. This technique has undergone promising developments to enable highly sensitive and specific measurements, leading to impressive demonstrations including that of definitive tissue identification, cancer diagnosis, and tumour margin delineation [143, 144]. The disadvantage however is that typically large tissue regions must be raster scanned point-by-point to gain spatial information (i.e. imaging in a spatially untargeted fashion) which requires numerous measurements and long acquisition times. Thus, mass spectrometers may benefit significantly from a targeted approach to broaden their clinical scope.

As discussed previously, existing modalities can be significantly enhanced with the hybridization of Mueller polarimeters. In a similar vein, Mueller measurements afford useful additional contrast mechanisms for cancer detection, and thus may be used to guide mass spectrometers to pathological areas, thereby avoiding unnecessary measurements and (importantly) significantly reducing examination times. Thus, Woolman et al. [55] have demonstrated Mueller polarimetric guidance of mass spectrometry, employing both transmission imaging of thin tissues and reflectance imaging of thick tissues, the latter being a precursor for in-vivo assessment. In their study, they examined lymph nodes with breast cancer involvement which exhibited both viable and necrotic regions. For validation reference, the thin tissue was histologically stained by H&E, revealing the two regions shown in Fig. 10f. Mueller-derived depolarization images of the thin (10 μm) and thick (50 μm) tissues are shown in Fig. 10a and b, exhibiting excellent contrast identification of the viable and necrotic regions in agreement with the H&E slide. The thin tissue polarimetric image was used to determine pathological and heterogeneous regions of interest (Fig. 10c) where guided mass spectrometry was performed (Fig. 10d). For comparison, much slower untargeted mass spectrometry of the entire thin tissue was performed (Fig. 10e), using two mass-to-charge ratios corresponding to viable (red, m/z 572.48) and necrotic (green, m/z 391.25) cancers. The latter took ~6 h, while the polarimetry-guided mass spectrometry took only ~8 min, a tremendous reduction in time. This is of considerable importance in the clinic, for example in intraoperative assessment of excised tumours to ensure all cancerous tissue has been removed (e.g. breast cancer surgical lumpectomy procedure with its rather short margin assessment window before the surgeon closes the wound). This study thus demonstrated the feasibility of polarimetric-guided mass spectrometry of thin and thick tissues. Further research on the latter should be performed to investigate the prospects of in vivo polarimetric mass-spec guidance. If successful, this approach may have significant impacts on surgical oncology and other clinical applications.

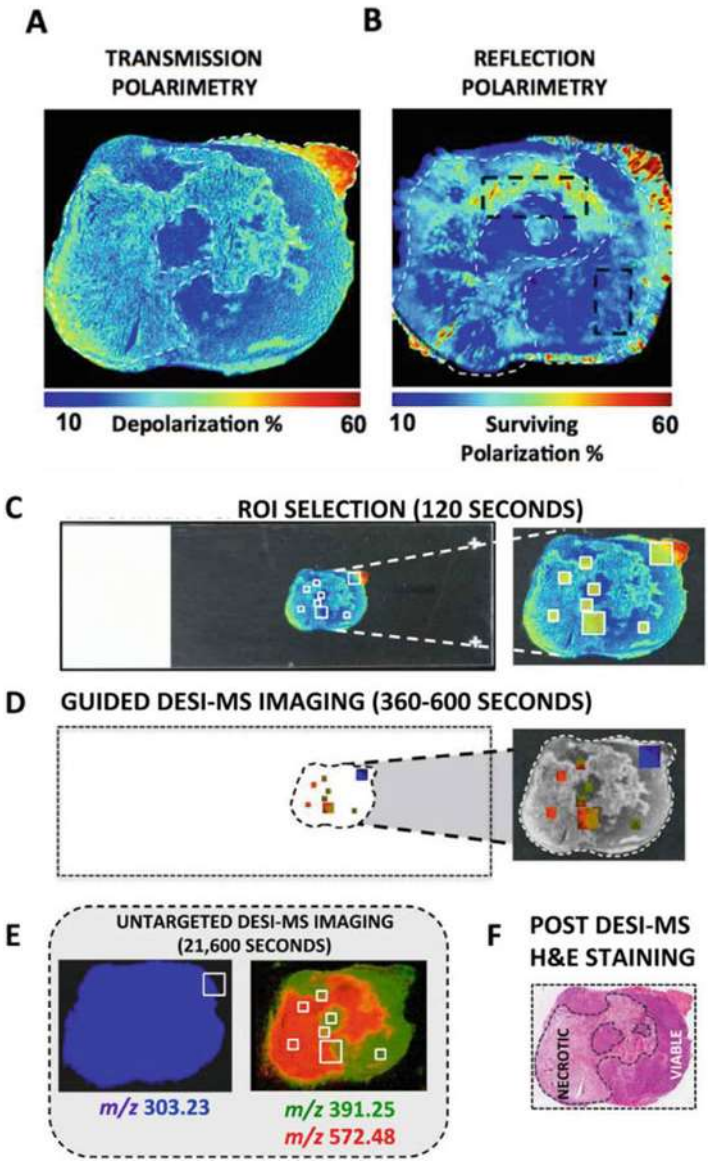


**Fig. 10** Optimization of mass spectrometry using Mueller polarimetric guidance. (From [55]). The examined tissue was a cancer infiltrated lymph node with viable and necrotic regions. Mueller depolarization image of thinly sliced tissue (10 μm) using transmission polarimetry (**a**) and of thick tissue (50 μm) using reflectance polarimetry (**b**). The latter is a feasibility test for polarimetric guidance on thick tissues, important for clinical applications such as margin assessment in breast lumpectomy patients. The depolarization images of both tissues show excellent contrast identification of viable and necrotic regions (see (**f**)). (**c**) Suspected regions of pathology and tissue heterogeneity are selected on the thin tissue sample using the depolarization image. (**d**) Mass spectrometry is performed on those polarimetrically targeted regions, with an acquisition time of ~8 min. (DESI-MS = Desorption Electrospray Ionization mass spectrometry) (**e**) Untargeted mass spectrometry is performed on the whole slide using two mass-to-charge ratios corresponding to viable (red, m/z 572.48) and necrotic (green, m/z 391.25) cancers. This was done in a much longer acquisition time of ~6 h. (**f**) H&E staining of the thin tissue sample as a validation reference, performed after the mass spectrometry step

### *4.3 Endoscopic Mueller Polarimetry*

The demonstrated tissue characterization potential of Mueller imaging, with its rich information content, non-invasive nature, and endogenous contrast, has prompted proposals for its use through optical fibres for endoscopic applications and surgical guidance. An excellent review of this topic has been written by Qi et al. [42] to which the reader may refer for details. Although in-vivo Mueller diagnostics can be done using free-space optics as in some of the preceding examples, the majority of bio-polarimetry applications have been performed ex vivo thus far. A key enabler towards wider in-vivo use will be fibre optic polarimetry, to gain significant access to human biology in various internal body cavities and orifices where many pathologies arise. The main challenge of this proposition is to overcome spurious polarization distortion artefacts introduced by (flexible) optical fibres. There also exists the 'usual' clinical engineering challenges of polarization generation and analysis in a practical manner (robustness, accuracy, speed, low complexity and cost, etc.).

To combat polarization distortion introduced by optical fibres (strain birefringence), the most effective solution thus far involves placing the polarization modulating components on the fibre's distal end. Qi et al. [145] used this approach to measure the linear 3 × 3 sub-matrix; this obviated the need for retarding components related to circular polarization generation and analysis, thereby simplifying the system. The information content of the linear sub-matrix, although less than that offered by the complete 4 × 4 MM, can still offer useful descriptions of sample properties such as scatterer concentration and size, as well as linear birefringence [146, 147]. To extract this information, the authors carried out the polar decomposition presented by Swami et al. [146] for 3 × 3 matrices. They then modified a rigid commercial endoscope consisting of an illumination channel with a linear polarizer affixed to its distal end, enabling the three linear states (horizontal, vertical, and 45°) to be generated by rotation of the entire fibre (motorized), and an imaging channel with a linear analyser placed before a CCD in the form of a rotating wheel containing three linear polarizers. The authors acquired depolarization and retardance images within a rat abdomen ex vivo in ~11.6 s, showing good discrimination between different organs as seen in Fig. 11a–c. It is thus clear that fibre optic MM polarimetry is feasible, at least in the context of a rigid endoscope. More information about this system will be provided in Chap. 7: Polarimetric Endoscopy.

Though the incomplete 3 × 3 Mueller polarimeter simplified the system design and reduced acquisition time, while also offering useful linear polarization-based information, measurement of the complete 4 × 4 MM is preferred since circular polarization also affords biomedically relevant information [91, 106, 148]. Qi and Elson [149] thus followed up with a complete fibre optic Mueller polarimeter using another rigid endoscope design utilizing a 'sheath' with motorized rotation. Its

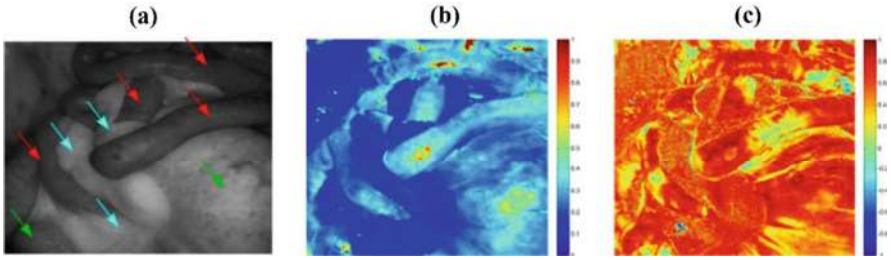


**Fig. 11** (**a**) unpolarized image of rat abdomen with red, green, and blue arrows indicating the small bowel, large bowel, and fat, respectively. (**b**) linear depolarization image showing distinction between bowel and fat. (**c**) linear retardance image showing weak(er) discrimination between organs. The 3 × 3 polar decomposition affords useful information through linear depolarization. The images were taken with 546 nm light with field of view of 5.5 × 5.5 $cm^2$. (From [145])

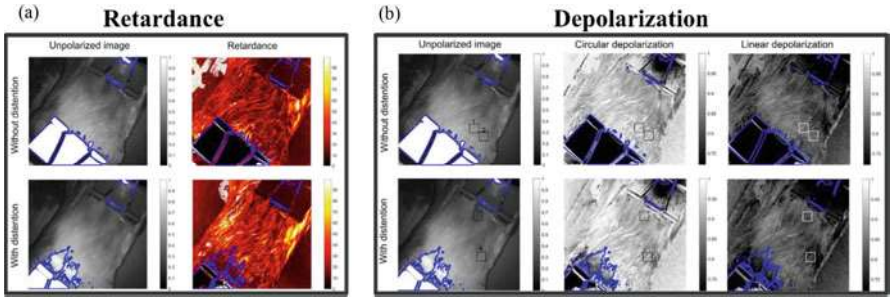


**Fig. 12** Retardance (right column) and unpolarized (left column) images of porcine bladders. The bladders were normal (top row) or distended (bottom row) in both (**a**) and (**b**). There is clear increase in retardance with distention of the bladder, arising from induced birefringence. (**b**) unpolarized (first column from the left, same as in (**a**)), circular depolarization (second column), and linear depolarization (third column) images of porcine bladders. Regions enclosed by the blue contours indicate pixel saturation in at least one of the raw images used for Mueller image retrieval. The field of view of images in (**a**) and (**b**) are 7.8 × 7.8 $cm^2$

distal end contained a ring-shaped retarding film affixed to the rotatable sheath which covered the illumination channel and a stationary linear polarizer covering both channels. Such a design is analogous to a free-space MM polarimeter with motor-rotated retarders and stationary linear polarizers. The acquisition time of this system was 30 s, currently limited by the rotation speed of the sheath. The resultant rigid Mueller polarimetric endoscope was used to image normal and stretched porcine bladders with high fidelity, shown in Fig. 12a and b. The bladder distention does not appear to affect linear or circular depolarization; however, the latter is evidently much stronger than the former. Comparison of linear and circular depolarization can be informative of the scattering properties of the material, for

example, Mie scatterers tend to preserve linear polarization better than circular, whereas the opposite occurs in the Rayleigh scattering regime [21, 80]. There is thus an advantage of measuring the complete 4 × 4 Mueller matrix rather than just its linear 3 × 3 sub-matrix counterpart.

For all the advantages of rigid endoscopes, including more manageable polarized-light artefacts, longer shelf life, and lower chromatic aberrations [44], they are limited to relatively easy-to-access clinical sites. Flexible endoscopes offer a clear advantage in this regard with their ability to 'snake' into many more inner orifices and cavities of the body, thus gaining diagnostic access to a wider array of pathologies. Flexible fibres however introduce the much more challenging variable strain birefringence when bending and twisting which causes significant polarization distortion. To address this issue, Forward et al. [44] placed stationary linear polarizers on the distal ends of the flexible optical fibres. Thus, any strain birefringence would manifest as changes in illumination intensity (i.e. light intensity after the polarizers), which, importantly, could be accounted for with their careful calibration procedure. In total, six fibres were used (fashioned into a single probe), the illumination and detection channels consisted of three fibres each to form a PSA and PSG, respectively, with three linear polarizer orientations for each channel: horizontal, vertical, and −45° (see Fig. 13). Pairwise combinations of the PSG and PSA components enabled the measurement of the linear 3 × 3 MM. The authors tested the flexible fibre's performance in point-sensing mode on simple optical elements as well as ex-vivo tissues. The next steps will be to measure the complete

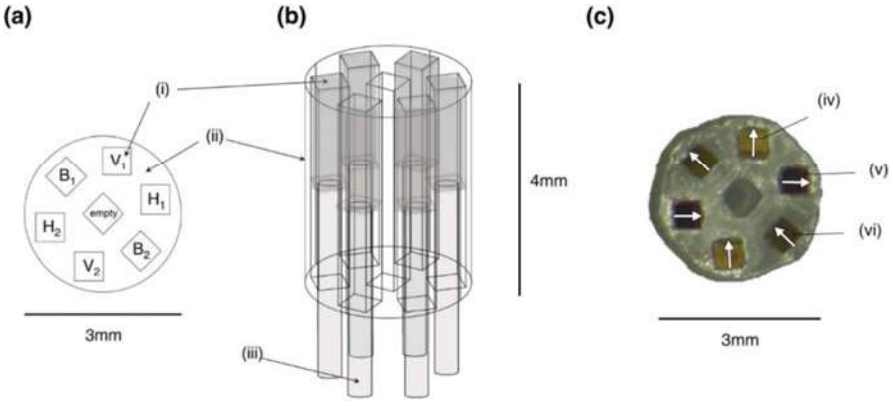


**Fig. 13** Flexible Mueller polarimeter with six internal fibres for measuring the 3 × 3 linear MM. (From [44]). (**a**) Top view schematic showing the six internal fibres. Three polarizer orientations are used on the distal ends of each fibre: horizontal ($H_{1,2}$), vertical ($V_{1,2}$), −45° ($B_{1,2}$). There were two of each polarization orientation, one set as the PSG and the other set as the PSA. (**b**) Side view three-dimensional schematic showing the design of the housing for the fibres. (**c**) Top view photograph of the complete probe with the six internal fibres labelled with arrows indicating their polarizer orientation (labels (i)–(vi) can be ignored here)

$4 \times 4$ MM, in imaging rather than point-sensing mode, to harness the full Mueller capabilities as illustrated previously. Optical fibre engineering advancements such as in-fibre dynamic polarization control [150] will likely accelerate progress towards these goals.

## 5 Summary and Future Outlook

Light has played an increasingly important role in biomedicine as a non-to-minimally invasive diagnostic tool by exploiting its many versatile properties. Practical utilization of these properties (e.g. modulation and detection) has relied heavily on the technologies of the day. Polarization is no exception; in fact, polarimetry is an excellent example of technology dependence to enable its deployment in the biomedical field. The major challenges of bio-polarimetry include (1) the weak signal effects from depolarization that must be overcome and (2) the complex and heterogeneous structure of tissues that must be deciphered. The information-rich Mueller matrix approach offers clear advantages with regard to (1) through various enabling technological advances and with regard to (2) through decomposition methods which can isolate the simultaneously occurring polarimetric effects. These advantages however come at a cost of measurement complexity (and associated lengthy acquisition times). Both the weak signal and measurement complexity challenges are being successfully addressed by enabling technologies and methodologies. Indeed, depolarization is becoming less of a hindrance and more of a diagnostic utility with the advent of more sensitive, robust, automated, and faster MM measurement systems.

With the challenges of MM tissue polarimetry steadily being addressed, its overall biomedical utility is finally at the stage of being properly evaluated. MM depolarization and retardance imaging presents strong contrast mechanisms between cancerous and non-cancerous tissues and may find a clinical niche in evaluating thin tissue slides to supplement current (expensive and often subjective) gold standard histopathological assessment. Additionally, rather invasive tissue biopsies for cancer detection may be reduced with the help of in-vivo polarimetric diagnostics, relying on bulk tissue retroreflection geometry deployments. In addition, although diattenuation has been thought to be of relatively little diagnostic value, it has recently shown some utility (e.g. burned bovine tendon study discussed previously). Optical activity, also amongst the weaker bio-polarimetric effects, may eventually be of significant clinical use in non-invasive glucose monitoring, which remains one of medicine's most pressing unsolved clinical needs. Overall then, MM polarimetry offers a suite of diagnostics options that are steadily finding their way into the biomedical arena.

It has also been shown that Mueller polarimeters can synergize with existing modalities through hybridization as seen in the combined OCT, SHG confocal microscopy, fluorescence microscopy, and mass spectrometry systems. Furthermore, the depth-resolved modalities can benefit Mueller polarimeters by providing

information on the often-problematic heterogeneous structure of tissue. The clinical scope of MM polarimetry may also be greatly extended through endoscopic techniques by enabling access to the interior of the various body cavities and orifices and hard-to-access anatomical sites where many pathologies arise. Additionally, the elusive prospect of detecting pre-cancer using polarized light [65, 66] may be significantly enhanced by probing sub-micron tissue structural anisotropy through multifractal analysis using MMs.

It seems that Mueller polarimetry is inextricably tied to both enabling technologies and novel methodologies which are increasingly extracting further biomedical diagnostic value from MMs. Far from having reached its potential in biomedicine (and other fields), MM polarimetry's true clinical prospects are arguably just beginning to emerge. Polarization – a fundamental property of light as well as one of the oldest to be studied – is thus beginning to earn its place amongst the more established optical diagnostic modalities in biomedicine, either alone or in combination, with exciting promise of selected clinical deployment in the near future.

## References

1. Goldstein, D.H.: Polarized light: a history. In: Polarized Light. CRC Press (2017)
2. Losurdo, M., Bergmair, M., Bruno, G., Cattelan, D., Cobet, C., de Martino, A., Fleischer, K., Dohcevic-Mitrovic, Z., Esser, N., Galliet, M., Gajic, R., Hemzal, D., Hingerl, K., Humlicek, J., Ossikovski, R., Popovic, Z.V., Saxl, O.: Spectroscopic ellipsometry and polarimetry for materials and systems analysis at the nanometer scale: state-of-the-art, potential, and perspectives. J. Nanopart. Res. **11**(7), 1521–1554 (2009)
3. Ghosh, N.: Tissue polarimetry: concepts, challenges, applications, and outlook. J. Biomed. Opt. **16**(11), 110801 (2011)
4. Stokes, G.G.: On the composition and resolution of streams of polarized light from different sources. Trans. Camb. Philos. Soc. **9**, 399 (1851)
5. Soleillet, P.: Sur les paramètres caractérisant la polarisation partielle de la lumière dans les phénomènes de fluorescence. Ann. Phys. (Paris). **10**(12), 23–97 (1929)
6. Perrin, F.: Polarization of light scattered by isotropic opalescent media. J. Chem. Phys. **10**(7), 415–427 (1942)
7. Mueller, H.: Memorandum on the polarization optics of the photoelastic shutter. Report No. 2 of the OSRD project OEMsr-576 (1943)
8. Jones, R.C.: A new calculus for the treatment of optical systems. V. A more general formulation, and description of another calculus. J. Opt. Soc. Am. **37**(2), 107 (1947)
9. Jones, R.C.: A new calculus for the treatment of pptical systems. I. Description and discussion of the calculus. J. Opt. Soc. Am. **31**(7), 488 (1941)
10. Hurwitz, H., Jones, R.C.: A new calculus for the treatment of optical systems. II. Proof of three general equivalence theorems. J. Opt. Soc. Am. **31**(7), 493 (1941)
11. Jones, R.C.: A new calculus for the treatment of optical systems. III. The Sohncke theory of optical activity. J. Opt. Soc. Am. **31**(7), 500 (1941)
12. Clark Jones, R.: A new calculus for the treatment of optical systems IV. J. Opt. Soc. Am. **32**(8), 486 (1942)
13. Pritchard, B.S., Elliott, W.G.: Two instruments for atmospheric optics measurements*. J. Opt. Soc. Am. **50**(3), 191 (1960)
14. Beardsley, G.F.: Mueller scattering matrix of sea water*. J. Opt. Soc. Am. **58**(1), 52 (1968)

15. Miller, R.H.: The effects of telescopes on astronomical polarization measurements. Appl. Opt. **2**(1), 61 (1963)
16. Tor, H.: A study of the depolarization of lunar radar echoes. Radio Sci. **2**(5), 445–465 (1967)
17. Bickel, W.S., Davidson, J.F., Huffman, D.R., Kilkson, R.: Application of polarization effects in light scattering: a new biophysical tool. Proc. Natl. Acad. Sci. U. S. A. **73**(2), 486–490 (1976)
18. Badoz, J.: Mesures photoélectriques de faibles biréfringences et de très petits pouvoirs rotatoires. J. Phys. Appl. **17**(S11), 143–149 (1956)
19. Billard, J.: Mise au point – Les modulateurs électro-optiques. Rev. Phys. Appl. **1**(4), 311–324 (1966)
20. Hielscher, A.H., Mourant, J.R., Bigio, I.J.: Influence of particle size and concentration on the diffuse backscattering of polarized light from tissue phantoms and biological cell suspensions. Appl. Opt. **36**(1), 125 (1997)
21. MacKintosh, F.C., Zhu, J.X., Pine, D.J., Weitz, D.A.: Polarization memory of multiply scattered light. Phys. Rev. B. **40**(13), 9342–9345 (1989)
22. Yoo, K.M., Alfano, R.R.: Time resolved depolarization of multiple backscattered light from random media. Phys. Lett. A. **142**(8–9), 531–536 (1989)
23. Bicout, D., Brosseau, C.: Multiply scattered waves through a spatially random medium: entropy production and depolarization. J. Phys. I. **2**(11), 2047–2063 (1992)
24. Schmitt, J.M., Gandjbakhche, A.H., Bonner, R.F.: Use of polarized light to discriminate short-path photons in a multiply scattering medium. Appl. Opt. **31**(30), 6535 (1992)
25. Dreher, A.W., Reiter, K., Weinreb, R.N.: Spatially resolved birefringence of the retinal nerve fiber layer assessed with a retinal laser ellipsometer. Appl. Opt. **31**(19), 3730 (1992)
26. Azzam, R.M.A.: Propagation of partially polarized light through anisotropic media with or without depolarization: a differential $4 \times 4$ matrix calculus. J. Opt. Soc. Am. **68**(12), 1756 (1978)
27. Ortega-Quijano, N., Arce-Diego, J.L.: Depolarizing differential Mueller matrices. Opt. Lett. **36**(13), 2429 (2011)
28. Ossikovski, R.: Differential and product Mueller matrix decompositions: a formal comparison. Opt. Lett. **37**(2), 220 (2012)
29. Ghosh, N., Wood, M., Vitkin, A.: Polarized light assessment of complex turbid media such as biological tissues using Mueller matrix decomposition. In: Handbook of Photonics for Biomedical Science, pp. 253–282. CRC Press (2010)
30. Lu, S.-Y., Chipman, R.A.: Interpretation of Mueller matrices based on polar decomposition. J. Opt. Soc. Am. A. **13**(5), 1106 (1996)
31. Smith, M.H., Burke, P.D., Lompado, A., Tanner, E.A., Hillman, L.W.: Mueller matrix imaging polarimetry in dermatology. In: Vo-Dinh, T., Grundfest, W.S., Benaron, D.A. (eds.) Biomedical Diagnostic, Guidance, and Surgical-Assist Systems II, vol. 3911, pp. 210–216 (2000)
32. Kumar, S., Purwar, H., Ossikovski, R., Vitkin, I.A., Ghosh, N.: Comparative study of differential matrix and extended polar decomposition formalisms for polarimetric characterization of complex tissue-like turbid media. J. Biomed. Opt. **17**(10), 105006 (2012)
33. Iqbal, M., Ahmad, I., Khaliq, A., Khan, S.: Comparative study of Mueller matrix transformation and polar decomposition for optical characterization of turbid media. Optik (Stuttg). **224**, 165508 (2020)
34. Tukimin, S.N., Karman, S.B., Ahmad, M.Y., Wan Kamarul Zaman, W.S.: Polarized light-based cancer cell detection techniques: a review. IEEE Sensors J. **19**(20), 9010–9025 (2019)
35. Aitken, K.J.: Optical assessment of tissue anisotropy in *ex vivo* distended rat bladders. J. Biomed. Opt. **17**(8), 086010 (2012)
36. Alali, S., Aitken, K.J., Schröder, A., Gribble, A., Bagli, D.J., Vitkin, I.A.: Assessment of local structural disorders of the bladder wall in partial bladder outlet obstruction using polarized light imaging. Biomed. Opt. Express. **5**(2), 621 (2014)
37. Wood, M.F.G., Ghosh, N., Wallenburg, M.A., Li, S.-H., Weisel, R.D., Wilson, B.C., Li, R.-K., Vitkin, I.A.: Polarization birefringence measurements for characterizing the myocardium,

including healthy, infarcted, and stem-cell-regenerated tissues. J. Biomed. Opt. **15**(4), 047009 (2010)
38. Ghosh, N., Alex Vitkin, I., Wood, M., Esenaliev, R.: Toward noninvasive glucose sensing using polarization analysis of multiply scattered light. In: Handbook of Optical Sensing of Glucose in Biological Fluids and Tissues, pp. 527–562. CRC Press (2008)
39. Sun, P., Ma, Y., Liu, W., Yang, Q., Jia, Q.: Mueller matrix decomposition for determination of optical rotation of glucose molecules in turbid media. J. Biomed. Opt. **19**(4), 046015 (2014)
40. Chen, T.-L., Lo, Y.-L., Liao, C.-C., Phan, Q.-H.: Noninvasive measurement of glucose concentration on human fingertip by optical coherence tomography. J. Biomed. Opt. **23**(04), 1 (2018)
41. Phan, Q.H., Jian, T.H., Huang, Y.R., Lai, Y.R., Xiao, W.Z., Chen, S.W.: Combination of surface plasmon resonance and differential Mueller matrix formalism for noninvasive glucose sensing. Opt. Lasers Eng. **134**, 106268 (2020)
42. Qi, J., Elson, D.S.: Mueller polarimetric imaging for surgical and diagnostic applications: a review. J. Biophotonics. **10**(8), 950–982 (2017)
43. Vizet, J., Manhas, S., Tran, J., Validire, P., Benali, A., Garcia-Caurel, E., Pierangelo, A., De Martino, A., Pagnoux, D.: Optical fiber-based full Mueller polarimeter for endoscopic imaging using a two-wavelength simultaneous measurement method. J. Biomed. Opt. **21**(7), 071106 (2016)
44. Forward, S., Gribble, A., Alali, S., Lindenmaier, A.A., Vitkin, I.A.: Flexible polarimetric probe for 3 × 3 Mueller matrix measurements of biological tissue. Sci. Rep. **7**(1), 11958 (2017)
45. Fu, Y., Huang, Z., He, H., Ma, H., Wu, J.: Flexible 3 × 3 Mueller matrix endoscope prototype for cancer detection. IEEE Trans. Instrum. Meas. **67**(7), 1700–1712 (2018)
46. Pierangelo, A., Manhas, S., Benali, A., Fallet, C., Antonelli, M.-R., Novikova, T., Gayet, B., Validire, P., De Martino, A.: Ex vivo photometric and polarimetric multilayer characterization of human healthy colon by multispectral Mueller imaging. J. Biomed. Opt. **17**(6), 066009 (2012)
47. Pierangelo, A., Manhas, S., Benali, A., Fallet, C., Totobenazara, J.-L., Antonelli, M.-R., Novikova, T., Gayet, B., De Martino, A., Validire, P.: Multispectral Mueller polarimetric imaging detecting residual cancer and cancer regression after neoadjuvant treatment for colorectal carcinomas. J. Biomed. Opt. **18**(4), 046014 (2013)
48. Pierangelo, A., Benali, A., Antonelli, M.-R., Novikova, T., Validire, P., Gayet, B., De Martino, A.: Ex-vivo characterization of human colon cancer by Mueller polarimetric imaging. Opt. Express. **19**(2), 1582 (2011)
49. Yao, G., Wang, L.V.: Two-dimensional depth-resolved Mueller matrix characterization of biological tissue by optical coherence tomography. Opt. Lett. **24**(8), 537 (1999)
50. Jiao, S., Wang, L.V.: Two-dimensional depth-resolved Mueller matrix of biological tissue measured with double-beam polarization-sensitive optical coherence tomography. Opt. Lett. **27**(2), 101 (2002)
51. Chue-Sang, J., Bai, Y., Stoff, S., Straton, D., Ramaswamy, S., Ramella-Roman, J.C.: Use of combined polarization-sensitive optical coherence tomography and Mueller matrix imaging for the polarimetric characterization of excised biological tissue. J. Biomed. Opt. **21**(7), 071109 (2016)
52. Chue-Sang, J., Bai, Y., Stoff, S., Gonzalez, M., Holness, N., Gomes, J., Jung, R., Gandjbakhche, A., Chernomordik, V.V., Ramella-Roman, J.C.: Use of Mueller matrix polarimetry and optical coherence tomography in the characterization of cervical collagen anisotropy. J. Biomed. Opt. **22**(08), 1 (2017)
53. Le Gratiet, A., Mohebi, A., Callegari, F., Bianchini, P., Diaspro, A.: Review on complete Mueller matrix optical scanning microscopy imaging. Appl. Sci. **11**(4), 1632 (2021)
54. Tata, A., Gribble, A., Ventura, M., Ganguly, M., Bluemke, E., Ginsberg, H.J., Jaffray, D.A., Ifa, D.R., Vitkin, A., Zarrine-Afsar, A.: Wide-field tissue polarimetry allows efficient localized mass spectrometry imaging of biological tissues. Chem. Sci. **7**(3), 2162–2169 (2016)

55. Woolman, M., Gribble, A., Bluemke, E., Zou, J., Ventura, M., Bernards, N., Wu, M., Ginsberg, H.J., Das, S., Vitkin, A., Zarrine-Afsar, A.: Optimized mass spectrometry analysis workflow with polarimetric guidance for ex vivo and in situ sampling of biological tissues. Sci. Rep. **7**(1), 1–12 (2017)
56. Lyle, R.E., Lyle, G.G.: A brief history of polarimetry. J. Chem. Educ. **41**(6), 308–313 (1964)
57. Vitkin, A.: POLARIZED LIGHT and the asymmetry of life. Opt. Photonics News. **7**(7), 30 (1996)
58. Jacques, S.L.: Polarized light imaging of biological tissues. In: Handbook of Biomedical Optics, pp. 649–668. CRC Press (2011)
59. He, H., Zeng, N., Du, E., Guo, Y., Li, D., Liao, R., Ma, H.: A possible quantitative Mueller matrix transformation technique for anisotropic scattering media. Photonics Lasers Med. **2**(2), 129–137 (2013)
60. He, H., Chang, J., He, C., Ma, H.: Transformation of full $4 \times 4$ Mueller matrices: a quantitative technique for biomedical diagnosis. In: Tuchin, V.V., Larin, K.V., Leahy, M.J., Wang, R.K. (eds.) Dynamics and Fluctuations in Biomedical Photonics XIII, vol. 9707, p. 97070K. SPIE (2016)
61. Quéau, Y., Leporcq, F., Lechervy, A., Alfalou, A.: Learning to classify materials using Mueller imaging polarimetry. In: Fourteenth International Conference on Quality Control by Artificial Vision, 111720Z, May 2019, Mulhouse, France. SPIE (2019)
62. Zhao, Y., Reda, M., Feng, K., Zhang, P., Cheng, G., Ren, Z., Kong, S.G., Su, S., Huang, H., Zang, J.: Detecting giant cell tumor of bone lesions using Mueller matrix polarization microscopic imaging and multi-parameters fusion network. IEEE Sensors J. **20**(13), 7208–7215 (2020)
63. Luu, N.T., Le, T., Phan, Q., Pham, T.-T.-H.: Characterization of Mueller matrix elements for classifying human skin cancer utilizing random forest algorithm. J. Biomed. Opt. **26**(07), 1–13 (2021)
64. Kudenov, M.W., Escuti, M.J., Hagen, N., Dereniak, E.L., Oka, K.: Snapshot imaging Mueller matrix polarimeter using polarization gratings. Opt. Lett. **37**(8), 1367 (2012)
65. Backman, V., Gurjar, R., Badizadegan, K., Itzkan, I., Dasari, R.R., Perelman, L.T., Feld, M.S.: Polarized light scattering spectroscopy for quantitative measurement of epithelial cellular structures in situ. IEEE J. Sel. Top. Quantum Electron. **5**(4), 1019–1026 (1999)
66. Gurjar, R.S., Backman, V., Perelman, L.T., Georgakoudi, I., Badizadegan, K., Itzkan, I., Dasari, R.R., Feld, M.S.: Imaging human epithelial properties with polarized light-scattering spectroscopy. Nat. Med. **7**(11), 1245–1248 (2001)
67. Jameson, D.M., Ross, J.A.: Fluorescence polarization/anisotropy in diagnostics and imaging. Chem. Rev. **110**(5), 2685–2708 (2010)
68. Guo, X., Wood, M.F.G., Vitkin, A.: A Monte Carlo study of penetration depth and sampling volume of polarized light in turbid media. Opt. Commun. **281**(3), 380–387 (2008)
69. Guo, X., Wood, M.F.G., Vitkin, A.: Monte Carlo study of pathlength distribution of polarized light in turbid media. Opt. Express. **15**(3), 1348 (2007)
70. Alali, S., Wang, Y., Vitkin, I.A.: Detecting axial heterogeneity of birefringence in layered turbid media using polarized light imaging. Biomed. Opt. Express. **3**(12), 3250 (2012)
71. Rehn, S., Planat-Chrétien, A., Berger, M., Dinten, J.-M., Deumié, C., da Silva, A.: Depth probing of diffuse tissues controlled with elliptically polarized light. J. Biomed. Opt. **18**(1), 016007 (2013)
72. Sridhar, S., Da Silva, A.: Enhanced contrast and depth resolution in polarization imaging using elliptically polarized light. J. Biomed. Opt. **21**(7), 071107 (2016)
73. Vashist, S.K.: Non-invasive glucose monitoring technology in diabetes management: a review. Anal. Chim. Acta. **750**, 16–27 (2012)
74. Ghosh, N.: Polarization birefringence measurements for characterizing the myocardium, including healthy, infarcted, and stem-cell-regenerated tissues. J. Biomed. Opt. **15**(4), 047009 (2010)
75. Riddell, R.H., Goldman, H., Ransohoff, D.F., Appelman, H.D., Fenoglio, C.M., Haggitt, R.C., Hren, C., Correa, P., Hamilton, S.R., Morson, B.C., Sommers, S.C., Yardley, J.H.:

Dysplasia in inflammatory bowel disease: standardized classification with provisional clinical applications. Hum. Pathol. **14**(11), 931–968 (1983)
76. Pupa, S.M., Ménard, S., Forti, S., Tagliabue, E.: New insights into the role of extracellular matrix during tumor onset and progression. J. Cell. Physiol. **192**(3), 259–267 (2002)
77. Mueller, M.M., Fusenig, N.E.: Tumor-stroma interactions directing phenotype and progression of epithelial skin tumor cells. Differentiation. **70**(9–10), 486–497 (2002)
78. Tuchin, V.V.: Polarized light interaction with tissues. J. Biomed. Opt. **21**(7), 071114 (2016)
79. Mourant, J.R., Johnson, T.M., Carpenter, S., Guerra, A., Aida, T., Freyer, J.P.: Polarized angular dependent spectroscopy of epithelial cells and epithelial cell nuclei to determine the size scale of scattering structures. J. Biomed. Opt. **7**(3), 378 (2002)
80. Bicout, D., Brosseau, C., Martinez, A.S., Schmitt, J.M.: Depolarization of multiply scattered waves by spherical diffusers: influence of the size parameter. Phys. Rev. E. **49**(2), 1767–1770 (1994)
81. Arifler, D., Pavlova, I., Gillenwater, A., Richards-Kortum, R.: Light scattering from collagen fiber networks: micro-optical properties of normal and neoplastic stroma. Biophys. J. **92**(9), 3260–3274 (2007)
82. Shukla, P., Pradhan, A.: Mueller decomposition images for cervical tissue: potential for discriminating normal and dysplastic states. Opt. Express. **17**(3), 1600 (2009)
83. Jacques, S.L., Roman, J.R., Lee, K.: Imaging superficial tissues with polarized light. Lasers Surg. Med. **26**(2), 119 (2000)
84. Chung, J., Jung, W., Hammer-Wilson, M.J., Wilder-Smith, P., Chen, Z.: Use of polar decomposition for the diagnosis of oral precancer. Appl. Opt. **46**(15), 3038–3045 (2007)
85. Saikia, B., Gupta, K., Saikia, U.N.: The modern histopathologist: in the changing face of time. Diagn. Pathol. **3**(1), 25 (2008)
86. Elmore, J.G., Barnhill, R.L., Elder, D.E., Longton, G.M., Pepe, M.S., Reisch, L.M., Carney, P.A., Titus, L.J., Nelson, H.D., Onega, T., Tosteson, A.N.A., Weinstock, M.A., Knezevich, S.R., Piepkorn, M.W.: Pathologists' diagnosis of invasive melanoma and melanocytic proliferations: observer accuracy and reproducibility study. BMJ. **357**, 2813 (2017)
87. Waldmann, A., Nolte, S., Geller, A.C., Katalinic, A., Weinstock, M.A., Volkmer, B., Greinert, R., Breitbart, E.W.: Frequency of excisions and yields of malignant skin tumors in a population-based screening intervention of 360 288 whole-body examinations. Arch. Dermatol. **148**(8), 903–910 (2012)
88. He, H., Dong, Y., Sheng, W., Ma, H.: Characterizing microstructural features of breast carcinoma tissues in different progression stages by transformed Mueller matrix parameters. Opt. InfoBase Conf. Pap. **Part F70-P**(8), 3643–3655 (2017)
89. Singh, M.D., Vitkin, I.A.: Discriminating turbid media by scatterer size and scattering coefficient using backscattered linearly and circularly polarized light. Biomed. Opt. Express. **12**(11), 6831–6843 (2021)
90. Pierangelo, A., Nazac, A., Benali, A., Validire, P., Cohen, H., Novikova, T., Ibrahim, B.H., Manhas, S., Fallet, C., Antonelli, M.-R., Martino, A.-D.: Polarimetric imaging of uterine cervix: a case study. Opt. Express. **21**(12), 14120 (2013)
91. Novikova, T., Pierangelo, A., Manhas, S., Benali, A., Validire, P., Gayet, B., De Martino, A.: The origins of polarimetric image contrast between healthy and cancerous human colon tissue. Appl. Phys. Lett. **102**(24), 241103 (2013)
92. Das, N., Chatterjee, S., Soni, J., Jagtap, J., Pradhan, A., Sengupta, T.K., Panigrahi, P.K., Vitkin, I.A., Ghosh, N.: Probing multifractality in tissue refractive index: prospects for precancer detection. Opt. Lett. **38**(2), 211 (2013)
93. Rehbinder, J., Deby, S., Haddad, H., Teig, B., Nazac, A., Pierangelo, A., Moreau, F.: Diagnosis of uterine cervix cancer using Müller polarimetry: a comparison with histopathology. Opt. InfoBase Conf. Pap. **9540**, 1–7 (2014)
94. Alali, S., Vitkin, A.: Polarized light imaging in biomedicine: emerging Mueller matrix methodologies for bulk tissue assessment. J. Biomed. Opt. **20**(6), 061104 (2015)
95. Vizet, J., Rehbinder, J., Deby, S., Roussel, S., Nazac, A., Soufan, R., Genestie, C., Haie-Meder, C., Fernandez, H., Moreau, F., Pierangelo, A.: In vivo imaging of uterine cervix with a Mueller polarimetric colposcope. Sci. Rep. **7**(1), 2471 (2017)

96. Sideri, M., Spolti, N., Spinaci, L., Sanvito, F., Ribaldone, R., Surico, N., Bucchi, L.: Interobserver variability of colposcopic, interpretations and consistency with final histologic results. J. Low. Genit. Tract Dis. **8**(3), 212–216 (2004)
97. Ramella-Roman, J.C., Gonzalez, M., Montejo, K., Chue-Sang, J., DeHoog, A., Madhivanan, P., Krup, K., Srinivas, V.: Development and characterization of a snapshot Mueller matrix polarimeter for the determination of cervical cancer risk in the low resource setting. In: Proceedings Volume 10485, Optics and Biophotonics in Low-Resource Settings IV, April 2018. SPIE (2018)
98. Gonzalez, M., Montejo, K.A., Krupp, K., Srinivas, V., DeHoog, E., Madhivanan, P., Ramella-Roman, J.C.: Design and implementation of a portable colposcope Mueller matrix polarimeter. J. Biomed. Opt. **25**(11), 1–16 (2020)
99. Jacques, S.L., Ramella-Roman, J.C., Lee, K.: Imaging skin pathology with polarized light. J. Biomed. Opt. **7**(3), 329 (2002)
100. da Silva, A., Stahl, P., Rehn, S., Vanzetta, I., Deumié, C.: Depth selectivity in biological tissues by polarization analysis of backscattered light. Opt. Complex Syst. OCS11. **8172**, 817205 (2011)
101. da Silva, A., Planat-Chrétien, A., Berger, M., Rehn, S., Dinten, J.-M., Deumié, C.: Probing biological tissues in depth with elliptically polarized light. In: Taroni, P., Dehghani, H. (eds.) Optics InfoBase Conference Papers, p. 879904. Optica Publishing Group (2013)
102. Rehn, S., Planat-Chrétien, A., Berger, M., Dinten, J.-M., Deumié, C., da Silva, A.: Comparison of polarized light penetration depth in scattering media. In: Hielscher, A.H., Taroni, P. (eds.) Optics InfoBase Conference Papers, p. 80881I. Optica Publishing Group (2011)
103. Da Silva, A., Deumié, C., Vanzetta, I.: Elliptically polarized light for depth resolved optical imaging. Biomed. Opt. Express. **3**(11), 2907 (2012)
104. Louie, D.C., Phillips, J., Tchvialeva, L., Kalia, S., Lui, H., Wang, W., Lee, T.K.: Degree of optical polarization as a tool for detecting melanoma: proof of principle. J. Biomed. Opt. **23**(12), 1 (2018)
105. Louie, D.C., Tchvialeva, L., Kalia, S., Lui, H., Lee, T.K.: Constructing a portable optical polarimetry probe for in-vivo skin cancer detection. J. Biomed. Opt. **26**(03), 1–15 (2021)
106. Kunnen, B., Macdonald, C., Doronin, A., Jacques, S., Eccles, M., Meglinski, I.: Application of circularly polarized light for non-invasive diagnosis of cancerous tissues and turbid tissue-like scattering media. J. Biophotonics. **8**(4), 317–323 (2015)
107. Anastasiadou, M., De Martino, A., Clement, D., Liège, F., Laude-Boulesteix, B., Quang, N., Dreyfuss, J., Huynh, B., Nazac, A., Schwartz, L., Cohen, H.: Polarimetric imaging for the diagnosis of cervical cancer. Phys. Status Solidi. **5**(5), 1423–1426 (2008)
108. Ivanov, D., Dremin, V., Bykov, A., Borisova, E., Genova, T., Popov, A., Ossikovski, R., Novikova, T., Meglinski, I.: Colon cancer detection by using Poincaré sphere and 2D polarimetric mapping of ex vivo colon samples. J. Biophotonics. **13**(8), 1–10 (2020)
109. Westreich, J., Khorasani, M., Jones, B., Demidov, V., Nofech-Mozes, S., Vitkin, A.: Novel methodology to image stromal tissue and assess its morphological features with polarized light: towards a tumour microenvironment prognostic signature. Biomed. Opt. Express. **10**(8), 3963 (2019)
110. Jones, B., Thomas, G., Westreich, J., Nofech-Mozes, S., Vitkin, A., Khorasani, M.: Novel quantitative signature of tumor stromal architecture: polarized light imaging differentiates between myxoid and sclerotic human breast cancer stroma. Biomed. Opt. Express. **11**(6), 3246 (2020)
111. Jones, B., Thomas, G., Sprenger, J., Nofech-Mozes, S., Khorasani, M., Vitkin, A.: Peritumoural stroma collagen organization of invasive ductal carcinoma assessed by polarized light microscopy differs between OncotypeDX risk group. J. Biophotonics. **13**(11), e202000188 (2020)
112. Mie, G.: Beiträge zur Optik trüber Medien, speziell kolloidaler Metallösungen. Ann. Phys. **330**(3), 377–445 (1908)
113. Das, N.K., Dey, R., Chakraborty, S., Panigrahi, P.K., Meglinski, I., Ghosh, N.: Quantitative assessment of submicron scale anisotropy in tissue multifractality by scattering Mueller matrix in the framework of Born approximation. Opt. Commun. **413**, 172–178 (2018)

114. Das, N.K., Dey, R., Ghosh, N.: Mueller matrix approach for probing multifractality in the underlying anisotropic connective tissue. J. Biomed. Opt. **21**(9), 095004 (2016)
115. Stanley, H.E., Meakin, P.: Multifractal phenomena in physics and chemistry. Nature. **335**(6189), 405–409 (1988)
116. Mandelbrot, B.B.: The Fractal Geometry of Nature. W. H. Freeman, New York (2000)
117. Ivanov, P.C., Amaral, L.A.N., Goldberger, A.L., Havlin, S., Rosenblum, M.G., Struzik, Z.R., Stanley, H.E.: Multifractality in human heartbeat dynamics. Nature. **399**(6735), 461–465 (1999)
118. Argoul, F., Arnéodo, A., Grasseau, G., Gagne, Y., Hopfinger, E.J., Frisch, U.: Wavelet analysis of turbulence reveals the multifractal nature of the Richardson cascade. Nature. **338**(6210), 51–53 (1989)
119. Kantelhardt, J.W., Zschiegner, S.A., Koscielny-Bunde, E., Havlin, S., Bunde, A., Stanley, H.E.: Multifractal detrended fluctuation analysis of nonstationary time series. Phys. A Stat. Mech. Appl. **316**(1–4), 87–114 (2002)
120. Das, N., Chatterjee, S., Kumar, S., Pradhan, A., Panigrahi, P., Vitkin, I.A., Ghosh, N.: Tissue multifractality and Born approximation in analysis of light scattering: a novel approach for precancers detection. Sci. Rep. **4**(1), 6129 (2015)
121. Das, N.K., Dey, R., Chakraborty, S., Panigrahi, P.K., Meglinski, I., Ghosh, N.: Submicron scale tissue multifractal anisotropy in polarized laser light scattering. Laser Phys. Lett. **15**(3), 035601 (2018)
122. Das, N.K., Dey, R., Chakraborty, S., Panigrahi, P.K., Ghosh, N.: Probing multifractality in depth-resolved refractive index fluctuations in biological tissues using backscattering spectral interferometry. J. Opt. **18**(12), 125301 (2016)
123. Mukhopadhyay, S., Das, N.K., Kurmi, I., Pradhan, A., Ghosh, N., Panigrahi, P.K.: Tissue multifractality and hidden Markov model based integrated framework for optimum precancer detection. J. Biomed. Opt. **22**(10), 1 (2017)
124. Lakowicz, J.R.: Principles of Fluorescence Spectroscopy. Springer (2006)
125. Arteaga, O., Nichols, S., Kahr, B.: Mueller matrices in fluorescence scattering. Opt. Lett. **37**(14), 2835 (2012)
126. Saha, S., Soni, J., Chandel, S., Kumar, U., Ghosh, N.: Probing intrinsic anisotropies of fluorescence: Mueller matrix approach. J. Biomed. Opt. **20**(8), 085005 (2015)
127. Jagtap, J., Chandel, S., Das, N., Soni, J., Chatterjee, S., Pradhan, A., Ghosh, N.: Quantitative Mueller matrix fluorescence spectroscopy for precancer detection. Opt. Lett. **39**(2), 243 (2014)
128. Satapathi, S., Soni, J., Ghosh, N.: Fluorescent Mueller matrix analysis of a highly scattering turbid media. Appl. Phys. Lett. **104**(13), 131902 (2014)
129. Soni, J., Purwar, H., Lakhotia, H., Chandel, S., Banerjee, C., Kumar, U., Ghosh, N.: Quantitative fluorescence and elastic scattering tissue polarimetry using an Eigenvalue calibrated spectroscopic Mueller matrix system. Opt. Express. **21**(13), 15475 (2013)
130. Maji, K., Saha, S., Dey, R., Ghosh, N., Haldar, D.: Mueller matrix fluorescence spectroscopy for probing self-assembled peptide-based hybrid supramolecular structure and orientation. J. Phys. Chem. C. **121**(35), 19519–19529 (2017)
131. Huang, D., Swanson, E., Lin, C., Schuman, J., Stinson, W., Chang, W., Hee, M., Flotte, T., Gregory, K., Puliafito, C., Et, A.: Optical coherence tomography. Science (80–). **254**(5035), 1178–1181 (1991)
132. Schmitt, J.M.: Optical coherence tomography (OCT): a review. IEEE J. Sel. Top. Quantum Electron. **5**(4), 1205–1215 (1999)
133. Ding, Z., Liang, C.-P., Chen, Y.: Technology developments and biomedical applications of polarization-sensitive optical coherence tomography. Front. Optoelectron. **8**(2), 128–140 (2015)
134. Hee, M.R., Swanson, E.A., Fujimoto, J.G., Huang, D.: Polarization-sensitive low-coherence reflectometer for birefringence characterization and ranging. J. Opt. Soc. Am. B. **9**(6), 903 (1992)

135. Cense, B., Chen, T.C., Mujat, M., Joo, C., Akkin, T., Park, B.H., Pierce, M.C., Yun, A., Bouma, B.E., Tearney, G.J., de Boer, J.F.: Spectral domain polarization-sensitive optical coherence tomography at 850 nm. In: Tuchin, V.V., Izatt, J.A., Fujimoto, J.G. (eds.) Coherence Domain Optical Methods and Optical Coherence Tomography in Biomedicine IX, vol. 5690, p. 159. SPIE (2005)
136. Götzinger, E., Pircher, M., Geitzenauer, W., Ahlers, C., Baumann, B., Michels, S., Schmidt-Erfurth, U., Hitzenberger, C.K.: Retinal pigment epithelium segmentation by polarization sensitive optical coherence tomography. Opt. Express. **16**(21), 16410 (2008)
137. Fukano, H., Matsuura, H., Hasegawa, Y., Nakamura, S.: Depth of invasion as a predictive factor for cervical lymph node metastasis in tongue carcinoma. Head Neck. **19**(3), 205–210 (1997)
138. Caldeira, P.C., Soto, A.M.L., Aguiar, M.C.F., Martins, C.C.: Tumor depth of invasion and prognosis of early-stage oral squamous cell carcinoma: a meta-analysis. Oral Dis. **26**(7), 1357–1365 (2020)
139. Fan, C., Yao, G.: Mapping local optical axis in birefringent samples using polarization-sensitive optical coherence tomography. J. Biomed. Opt. **17**(11), 110501 (2012)
140. Campagnola, P.J., Loew, L.M.: Second-harmonic imaging microscopy for visualizing biomolecular arrays in cells, tissues and organisms. Nat. Biotechnol. **21**(11), 1356–1360 (2003)
141. Okoro, C., Kelkar, V., Sivaguru, M., Emmadi, R., Toussaint, K.C.: Second-harmonic patterned polarization-analyzed reflection confocal microscopy of stromal collagen in benign and malignant breast tissues. Sci. Rep. **8**(1), 16243 (2018)
142. Saytashev, I., Saha, S., Chue-Sang, J., Lopez, P., Laughrey, M., Ramella-Roman, J.C.: Self validating Mueller matrix Micro–Mesoscope (SAMMM) for the characterization of biological media. Opt. Lett. **45**(8), 2168 (2020)
143. Ifa, D.R., Eberlin, L.S.: Ambient ionization mass spectrometry for cancer diagnosis and surgical margin evaluation. Clin. Chem. **62**(1), 111–123 (2016)
144. Balog, J., Sasi-Szabo, L., Kinross, J., Lewis, M.R., Muirhead, L.J., Veselkov, K., Mirnezami, R., Dezso, B., Damjanovich, L., Darzi, A., Nicholson, J.K., Takats, Z.: Intraoperative tissue identification using rapid evaporative ionization mass spectrometry. Sci. Transl. Med. **5**(194), 194ra93 (2013)
145. Qi, J., Ye, M., Singh, M., Clancy, N.T., Elson, D.S.: Narrow band $3 \times 3$ Mueller polarimetric endoscopy. Biomed. Opt. Express. **4**(11), 2433 (2013)
146. Swami, M.K., Manhas, S., Buddhiwant, P., Ghosh, N., Uppal, A., Gupta, P.K.: Polar decomposition of 3 x 3 Mueller matrix: a tool for quantitative tissue polarimetry. Opt. Express. **14**(20), 9324 (2006)
147. Wang, Y., Guo, Y., Zeng, N., Chen, D., He, H., Ma, H.: Study on the validity of $3 \times 3$ Mueller matrix decomposition. J. Biomed. Opt. **20**(6), 065003 (2015)
148. Wang, W., Lim, L.G., Srivastava, S., Yan, J.S.B., Shabbir, A., Liu, Q.: Roles of linear and circular polarization properties and effect of wavelength choice on differentiation between ex vivo normal and cancerous gastric samples. J. Biomed. Opt. **19**(4), 046020 (2014)
149. Qi, J., Elson, D.S.: A high definition Mueller polarimetric endoscope for tissue characterisation. Sci. Rep. **6**, 1–11 (2016)
150. Rahnama, A., Dadalyan, T., Mahmoud Aghdami, K., Galstian, T., Herman, P.R.: In-fiber switchable polarization filter based on liquid crystal filled hollow-filament Bragg gratings. Adv. Opt. Mater. **9**(19), 2100054 (2021)